České vysoké učení technické v Praze
Fakulta jaderná a fyzikálně inženýrská
Katedra fyziky
Experimentální jaderná a částicová fyzika

Výzkumný úkol na téma:

Výpočet korekce k určení přesné polohy dopředného detektoru v experimentu ATLAS

Autor: Bc. David Gančarčík
Školitel: Ing. Miroslav Myška, Ph.D.

Praha, Srpen 2020

Školitel:

Ing. Miroslav Myška, Ph.D.
Katedra fyziky Fakulta jaderná a fyzikálně inženýrská
Břehová 78/7
Staré Město, 115 19
Czech Republic

Czech Technical University in Prague
Faculty of Nuclear Sciences and Physical Engineering
Department of Physics
Experimental Nuclear and Particle Physics

Research thesis on topic:

Determination of correction for precise alignment of forward detector in the ATLAS experiment

Autor: Bc. David Gančarčík
Supervisor: Ing. Miroslav Myška, Ph.D.

Prague, August 2020

Supervisor:
Ing. Miroslav Myška, Ph.D.
Department of Physics Faculty of Nuclear Sciences and Physical Engineering
Břehová 78/7
Staré Město, 115 19
Czech Republic

Prohlášení

Prohlašuji, že jsem svou bakalářskou práci vypracoval samostatně a použil jsem pouze podklady (literaturu, projekty, SW atd.) uvedené v přiloženém seznamu.

Nemám vůbec žádný důvod proti použití této práce ve smyslu § 60 Zákona č. 121/2000 Sb., o právu autorském, o právech souvisejících s právem autorským a o změně některých zákonů (autorský zákon).

V Praze dne 1/9/2020 .....

.....
David Gančarčík

Poděkování

Tímto bych chtěl ze srdce poděkovat svému školiteli Ing. Miroslavu Myškovi Ph.D. za vědomosti, které mi předal a za čas, který strávil při pomoci s psaním této práce. Dále pak za všechnu rady, které mi udělil jak už spojené s touto prací tak i všeobecně. Dále bych rád poděkoval Rafałovi Staszewski Ph.D. za objasnění všech nejasností ohledně této prace, za rady ohledně kódu a vůbec se vším spojeným s uvedenou analýzou. Dále bych rád poděkoval svým rodičům za podporu, při mých studích a za vše ostatní. V neposlední řadě bych rád poděkoval své manželce za pomoc s úpravou obrázku a hlavně za podporu při psaní této prace. Nakonec bych rád poděkoval své dceři za dodání motivace.

ČESKÉ VYSOKÉ UČENÍ TECHNICKÉ V PRAZE
FAKULTA JADERNÁ A FYZIKÁLNĚ INŽENÝRSKÁ
PRAHA 1 - STARÉ MĚSTO, BŘEHOVÁ 7 - PSČ 115 19

Katedra: fyziky **Akademický rok:** 2019/2020

VÝZKUMNÝ ÚKOL

Student: **Bc. David Gančarčík**

Studijní program: **NMS**

Obor: **EJČF**

Vedoucí úkolu: Ing. Miroslav Myška, Ph.D.

Název úkolu (česky/anglicky): Výpočet korekce k určení přesné polohy dopředného detektoru v experimentu ATLAS. / Determination of correction for precise alignment of forward detector in the ATLAS experiment.

Pokyny pro vypracování:
Motivací pro tuto práci je měření exkluzivních událostí v proton-protonových srážkách v experimentu ATLAS. K určení plného koncového stavu, například k měření rozptýlených protonů, je třeba detailně porozumět nastavení dopředného detektoru AFP (Atlas Forward Proton), který je integrální součást experimentu ATLAS. V práci vypracujte změření pozice křemíkových detektorů AFP vzhledem k ose urychlovačové trubice metodou nejužšího rozložení odezvy detektoru (hot-spot method). K dispozici je několik pomocných statistických nástrojů v programu ROOT či jeho knihovny RooFit. Získané výsledky předneste pracovní skupině Soft QCD a AFP.

Součástí zadání výzkumného úkolu je jeho uložení na webové stránky katedry fyziky.

Literatura:

1. Adamcyk. A. et al., Technical Design Report for the ATLAS Forward Proton Detector, CERN-LHCC-2015-009; ATLAS-TDR-024; 2015
2. The ATLAS Collaboration, Proton tagging with the one arm AFP detector, ATL-PHYS-PUB-2017-012
3. The ATLAS Collaboration, Exclusive muon pair production at 13 TeV, Phys. Lett. B 777 (2018) 303
4. Buglewicz P. and Staszewski R., Hot-spot Method for Alignment of Forward Proton Detectors at the LHC, Acta Phys. Polon. B47 (2016) 1619-1624.

Datum zadání: 25.10.2019 ……..……

Datum odevzdání: 26.06.2020 ***vedoucí katedry***

Název práce:

Výpočet korekce k určení přesné polohy dopředného detektoru v experimentu ATLAS

Autor: Bc. David Gančarčík

Obor: Experimentální jaderná a částicová fyzika
Druh práce: Výzkumný úkol

Abstrakt: Tato práce se zabývá určením přesné pozice dopředného detektoru AFP, který je součástí experimentu ATLAS. V teoretické části této práce je shrnuta základní myšlenka organizace CERN. Dále jsou pak v práci popsány experimenty, které pod tento výzkumný ústav spadají. Následuje popis urychlovače LHC, detetoru ATLAS a všech jeho podpurných systémů. Zde jsou popsány i magnety, které tvoří optiku urychlovače. Dále se práce zabývá detektorem AFP. Jsou uvedeny jeho specifikace a také na jakém principu detektor funguje. Dále jsou zmíněny některé z metod pro výpočet polohy tohoto detektoru. Nakonec je popsán postup, jak byla provaděna analýza metody Hot-spot na datech ze specialniho runu. Výsledky jsou pak porovnány se simulací. Korekce k určení přesné polohy každé stanice dopředného detektoru AFP se nachází na konci práce.

Key words: CERN, ATLAS, AFP, částicová fyzika

Title:

Determination of correction for precise alignment of forward detector in the ATLAS experiment

Author: Bc. David Gančarčík

Field of studies: Experimental Nuclear and Particle Physics
Type of thesis: Research project

Abstract: This thesis deals with problem of finding precise position of the AFP detector being one of the forward detector of the ATLAS experiment. In the theoretical part of this thesis is the goal CERN organization described and the experiments that are part of it. Afterwards the detailed description of the LHC and the ATLAS detector plus its surrounding parts are discussed. The LHC magnet lattice is discussed. Then the AFP detector is described. After its constituents also the way how it measures the scattered proton is clarified. The principle two other alignment methods are discussed. Finally the Hot-spot alignment method is performed on data from special run. The results are compared to the simulation. The correction for the precise alignment of each station of the forward detector AFP is situated at the end of the thesis.

Key words: CERN, ATLAS, AFP, particle physics

Contents

Contents

Introduction

When two beams of the protons collide at centre of the ATLAS detector, most of the time no hard process occurs. When the interaction involve exchange of the colour-less object and a process called diffraction takes place, the protons could not be measured. They either dissociate into higher-mass state or they stay intact. But they are scattered into small angle and goes back into the beampipe. Because of this fact the dedicated detector systems are build far away from collision point. Those can measure the scattered protons because they are inserted straight into the beampipe. The AFP detector is one of them. Its both arms are more than $200\ \mathrm{m}$ far away from the central detector.

It consist of a Silicon tracker detector and a Time-of-Flight detector. The exact position of the tracker is must for the precise momentum measurement. A several methods were developed to found this position. Some of them rely on reconstruction of produced particles in the central detector. An interesting fact is that method presented in this thesis takes the information just from the AFP detector and also that the precision could be found for each part of the detector independently.

First part of this thesis will introduce the physics studied by the CERN organization, LHC accelerator and its optics. All main parts of the ATLAS central detector will be described in detail, together with the forward detectors surrounding it. Since this thesis deals mainly with the AFP detector, all its parts will be described. One local and one global alignment method will be mentioned.

Last part of the thesis aims to describe the Hot-spot global alignment method. The gathering of data from the scratch disk, reconstruction of the RAW data, analysing the data using toolbox developed by the AFP collaboration will be the goal of the thesis. Then is plan of action to find the Hot-spot position on binned data using the ROOT analysis framework. If this procedure will not be satisfactory (the precision of the method will be in orders hundreds of μm) the unbinned version approach will be performed using the RooFit. Obtained results from both the MC and the data will be compared. Then the corrections to each station of the AFP detector position will be found.

CHAPTER 1

ATLAS

1.1 CERN

European Council for Nuclear Research (Conseil Européen pour la Recherche Nucléaire) was a provisional council based in 1952. In 1954 the European Organisation for Nuclear Research was founded by order of the war destroyed Europe after World War II. The organisation shall not work for militarily requirements and all results shall be generally available. There was 12 member states from western Europe. Later more states from all over the world joined the organisation. The Czech Republic became a member in 1993. Today CERN has 23 member states, 6 associate member states, Cyprus and Slovenia are in the pre-stage to membership and Japan, the Russian Federation, the United States, European Union and UNESCO currently have observer status. The mission is to provide a wide range of particle accelerator facilities that allow research of fundamental physics on world-class level also as connect the people from all over the world and push the limits of science and technology for the benefit of all.

CERN is situated at Franco-Swiss border close to the Geneva. The highest authority of the organization is CERN Council. It is the head of the Organization that determines the policy in technical, scientific and administrative matters. It leads all strategic programmes and also approves the budget. Funding of CERN for the year 2020 is on Fig. 1.1. Director-General (currently Fabiola Gianotti) is appointed by the council. Each member state has a two delegates for representation of the government and national scientific interests. There is equally a single vote for every country. CERN council meets usually four times a year. Scientific Policy Committee and Finance Committee assist the council. There is around 2,500 staff members plus around 13,000 users from all around the world, who help with preparation of experiments and analyse of the measured data.

To study subnuclear physics, one needs particles with energy higher than could be delivered from decay of radioactive elements. Cosmic radiation has this ability, but the intensity is not sufficient for the charged particles (except widely used cosmic muons). Because of this fact particle accelerators are needed.

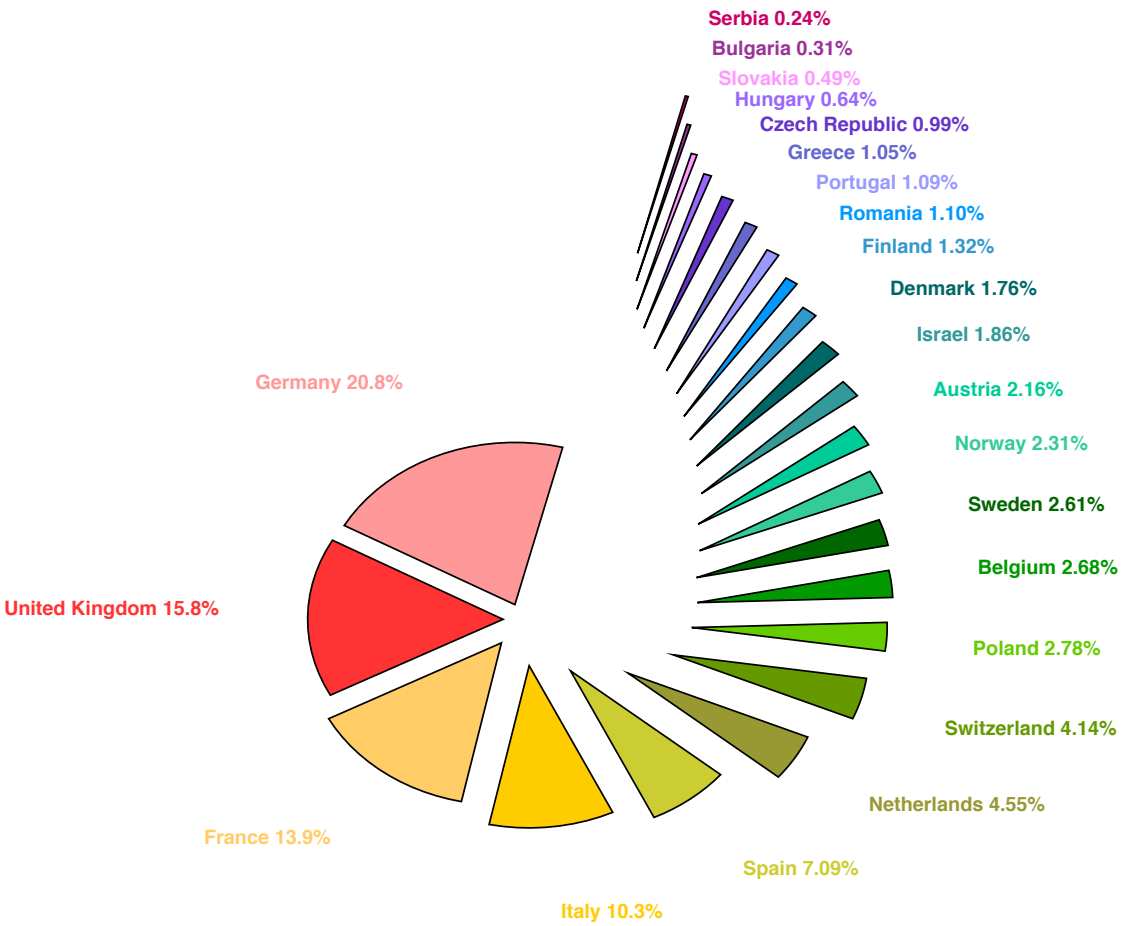

Figure 1.1: 2020 annual contributions to CERN budget.

Particle accelators could be sorted to linar and circular ones. Currently there are three operating LINACs (LINear ACcelerators) at CERN, namely LINAC2, LINAC3, LINAC4. The oldest and still active LINAC2 was build in 1978, as substitution for LINAC1. It was able to deliver higher intensity beams then its forerunner. Protons come to LINAC2 from hydrogen bottle, they pass through stripping foil, where the electron is stripped. Proton beam passes through the conductors, charged by radiofrequency cavities. Small quadrupole magnets ensure the beam is tight. LINAC2 speed up protons to energy $50\ \mathrm{MeV}$. LINAC3 was constructed inside the former tunnel of LINAC1 [1]. It is source of ions used at CERN (mainly lead but might be substituted by xenon or argon). It works on same basis as LINAC2 except magnets focusing the beam needs to be more powerful. LINAC4 will replace LINAC2 this year [2]. Instead of directly accelerating protons it uses H^- as a source and after boosting them into energy $160\ \mathrm{MeV}$ they are directed straight to SPS, where both electrons are lost and only hydrogen nuclei (proton) remains [3]. This procedure simplifies injection and keeps the population of protons higher. CLEAR is research development study accelerator for existing and possible future machines at CERN [4].

The LEIR (Low Energy Ion Ring) was first proposed in 1993 as a extension of a then-existing machine LEAR (Low Energy Antiproton Ring) [5]. The older machine was build to slow

down the antiprotons (nowaday this purpose is covered by the Antiproton Decelerator and with experiments ALPHA, AEGIS and ASACUSA). It receives long pulses of lead ions from LINAC3 and transforms them into the short, dense bunches suitable for injection in to the LHC. The Proton Synchrotron Booster (PSB) is made up of four synchrotron rings. It gets protons from the LINAC2 at $50\ \mathrm{MeV}$ and boost them to energy $1.4\ \mathrm{GeV}$. The PSB allows the PS (Proton Synchrotron) to accept over 100 times more protons compared to situation before PSB was build and proton beams were injected straight to PS. The CERN flagship PS is circular proton or ion synchrotron, that has been working since 1959 [6]. With a radius of $100\ \mathrm{m}$, the PS has 277 room-temperature electromagnets, including 100 dipoles to bend the particles. It could accelerate many types of particles (protons, alpha particles, oxygen or sulphur nuclei, electrons, positrons and anti-protons). Using a neutrino beam produced by a proton beam from PS, the Gargamelle experiment discovered weak neutral current and thus indirectly proved the existence of a neutral particle to carry the weak fundamental force in 1973 [7]. The AD (Antiproton Decelerator) is a unique machine producing anti-protons with low energy. It uses the beam from PS and smashes it into a block of metal [8]. This induces many particles including anti-protons that are separated. ELENA is ring dedicated to slow down anti-protons gained from AD. Those decreased anti-protons are forced to mix with positrons to make an anti-hydrogen. Goal is to perform anti-hydrogen spectroscopy and explore the effect of the gravitational force on matter and anti-matter. The Super Proton Synchrotron (SPS) is the $7\ \mathrm{km}$ long circular accelerator active since 1976. Particles from the PS are guided to SPS, where they are accelerated to the energy of $450\ \mathrm{GeV}$. There is 1317 room-temperature electromagnets in SPS, including 744 dipoles for bending. SPS could be turned to $p\overline{p}$ (proton-antiproton) collider. This setting won a Nobel price in 1983 for discovery of W and Z particles. So far SPS provide beams for the LHC (Large Hadron Collider), the NA61/SHINE and NA62 experiments, the COMPASS and AWAKE experiment. NA61/SHINE experiment studies the hadron production properties in collisions of protons, pions or even argon, beryllium or xenon nuclei with many different types of fixed targets. NA62 studies how protons delivered by SPS decay to kaons. COMPASS experiment explores the structure of hadrons using beam from SPS.

AWAKE experiment investigates the accelerating of charged particles by plasma wakefields [9]. It uses proton beams from SPS and injects them into a plasma to gain strong wakefields. A second beam is then accelerated by the wakefields, up to several GeV energy. The transition between hadrons and so-called quark-gluon plasma is studied in SHINE experiment. The CLOUD experiment uses special cloud chamber that can make a temperature and conditions same as in the atmosphere. It looks for a possible link between cosmic rays and cloud formation. CAST experiment is equipped with a telescope to search for theoretical particles called axions. The telescope is build of LHC dipole magnet acting as viewing tube. All of the accelerators, decelerators and particle detectors are located in Geneva region except AMS (Alpha Magnetic Spectrometer). AMS is situated on ISS (International Space Station) and measures antimatter in cosmic rays.

1.2 LHC

> One's awe is overlaid by the knowledge that the peoples of the world have come together to explore the deepest secrets of nature, something quite inspiring and stunning in itself.
>
> **The Large Hadron Collider**
> ***Andrew J Millington*** [10]

It is world's biggest and most powerful particle accelerator for more than ten years now. It collided two bunches for the first time on 10 September 2008. CERN's accelerator cascade was described in previous section and it could be also seen on Fig. 1.2. This thesis will focus on LHC as a $p\overline{p}$ collider and do not mind other possibilities (such as proton-ion or ion-ion collider) [11].

In the very first stage the electron is stripped of the hydrogen atom. The arising protons are accelerated by LINAC2 and guided to PSB. Later on, as they speed up, protons are injected into PS, SPS and then finally into the LHC, where they gain energy of $6.5\ \mathrm{TeV}$. This means that they travel about $3.1\ \mathrm{m/s}$ slower, then light in vacuum. Bunches of protons travel in LHC beampipe in both clockwise and counterclockwise direction. They collide in almost head-on collision on 4 spots of LHC ring called IP (Interaction Points), where four main experiments are based. This non-zero angle is called crossing angle.

The LHC tunnel (formerly used to house LEP collider) is $26.7\ \mathrm{km}$ long, at a depth ranging from $50 - 175\ \mathrm{m}$. When LHC is in full operation, it is filled with more than $2,800$ bunches. They travel in beampipe at discrete intervals of $25\ \mathrm{ns}$, so the bunch collision rate is $f = 40\ \mathrm{MHz}$ (40 million bunch crossing per second at each IP). The power of LHC could be quantified with luminosity $\mathcal{L}$, defined as

$$\mathcal{L} = f\frac{N^2}{4\pi\sigma_x\sigma_y}, \tag{1.1}$$

where f is frequency of colliding bunches, N is number of proton in one bunch (we assume that both colliding bunches have same population of protons), σ_x and σ_y are respectively transverse beam sizes in the horizontal and vertical directions. Luminosity gives number of collisions that can be produced in a detector per cm^2 and per second. When machine is working it draws around $200\ \mathrm{MW}$ of electrical power. In order to accelerate the protons we need a longitudinal electric field. Oscillating voltage is used, so that the particle is only affected by an accelerating voltage at the gap, and the voltage then cancels out as the particle goes around the rest of the ring. There is 1232 dipole magnets that keep protons on right circular path and additional 392 quadrupole magnets, that are used for focusing of the bunches. Because the principle of magnet operation will be useful for this thesis, it will be described closer in following subsection.

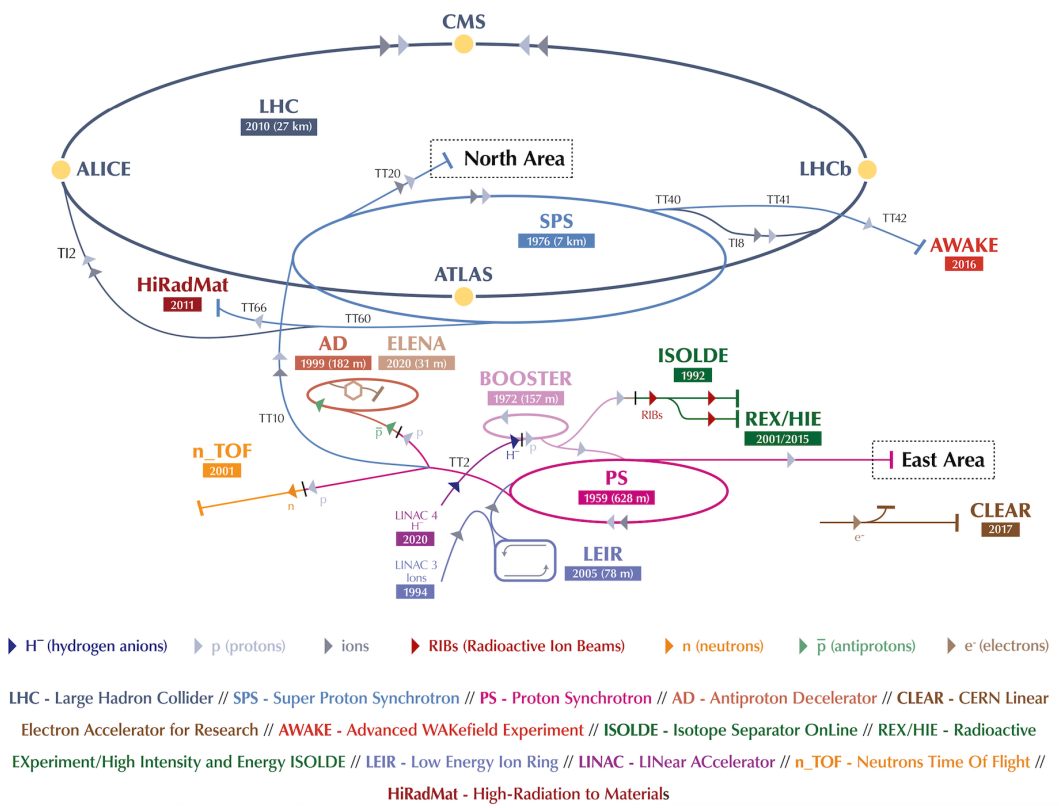

Figure 1.2: CERN accelerator cascade [12].

1.2.1 Magnets

They are the key components, when a new collider is build. From assumption of equivalence of magnetic and centripetal force one can get a relation

$$|\vec{p}| = qR|\vec{B}| \tag{1.2}$$

between momentum $\vec{p}$, charge q, radius R and magnetic field $\vec{B}$. This equation says that if one wants to increase the momentum of colliding particle one has to make a bigger collider (in means of bigger R) or we have to make magnets stronger. Focusing and bending could be done using electrical or magnetic force. In accelerators it is usually magnetic one. One introduces Lorentz force as

$$F_L = q(\vec{E} + \vec{v} \times \vec{B}), \tag{1.3}$$

where $\vec{v}$ is velocity and $\vec{E}$ is electric field acting on the particle. For particles traveling really fast $|\vec{v}| \approx c$ is magnetic field much more effective. Benefits also come from the fact, that magnetic force exerted on particle is always perpendicular to its velocity. All magnets are cooled down by superfluid helium to temperature 1.8 K to become superconducting [13]. Magnets could be classified according to number of poles they contain. Magnets with two poles are called dipole magnets, quadrupoles with four poles focus the beam. They are imperfect so one comes with sextupoles that correct its job. There are also higher order magnets used in LHC such as octupoles and so on.

Dipole magnets

There are two separated beams going in two tubes in opposite direction and both of them needs to be bend. The strong dipole magnetic field is achieved using superconducting cables around each beampipe in the LHC [14]. There are two layers of cables around each tube, that circulate in opposite sense summing the magnetic field induced by current. The magnet is wound of a superconductive cables, with strands made of nobium-titanium filaments surrounded by cooper matrix [15]. Fig. 1.3 shows the cross-section of LHC dipole magnet.

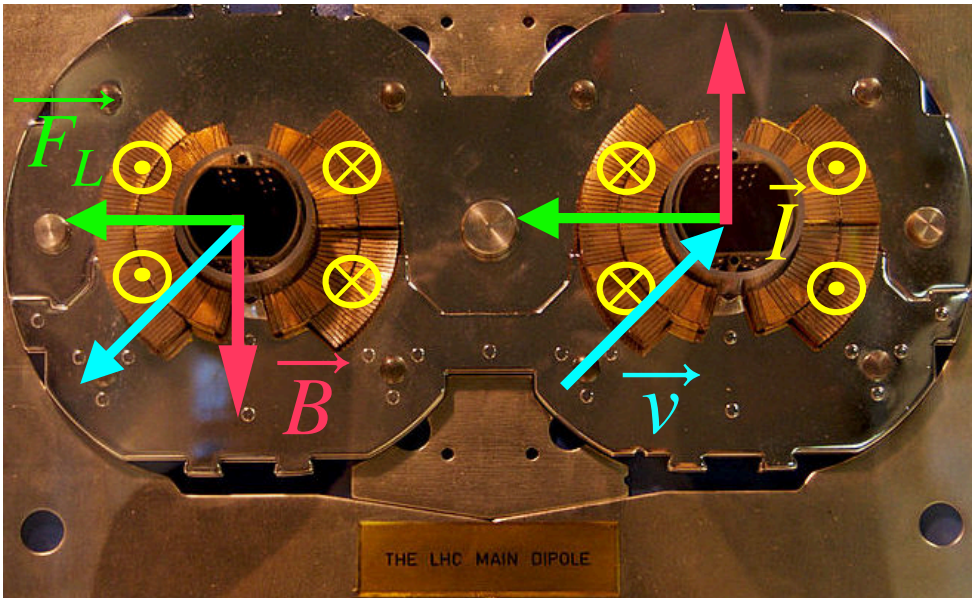

Figure 1.3: LHC main dipole magnet [12]. The current $\vec{I}$ (coloured in yellow) is flowing in opposite direction around each beampipe. Directions are swooped for each pipe, because bunches of particles going in opposite direction (velocity colored in cyan). This cause opposite direction of magnetic field $\vec{B}$ (red colour) the Lorenz force $\vec{F}_L$ over both beams act in same direction (towards centre of LHC). Photo taken from [16].

Quadrupole and higher order magnets

Protons are charged particles, so they repulse each other. Because of this fact one has to focus them and keep transverse beam size as small as possible (to increase the $\mathcal{L}$). Quadrupole and higher order magnets do the job for us. Quadrupoles act on beam of charged particles in the very same way as lens acts on beam of light [17]. It focuses the beam in one direction and spreads it in the other one. That is the reason, why two quadrupoles are coupled in the row, where the second one is $90°$ rotated around the axis of beampipe. Because of enormous number of protons in each bunch (around 10^{11}), the energy is little bit different for each proton so they are following slightly different paths. The sextupole and higher order magnets are able to focus the particles according to their energy.

1.3 ATLAS

There are four major experiments operating on the LHC. ALICE (A Large Ion Collider Experiment) focuses on the interactions of heavy ions. The goal of this project is to explore the physics of strong interaction and the new phase of matter, the quark-gluon plasma. LHC-b (Large Hadron Collider beauty experiment) has a mission to study CP violation in decays of hadrons containing heavy quarks. ATLAS (A Toroidal LHC ApparatuS) and CMS (Compact Muon Solenoid) are called the "general-purpose detectors". The goal of those experiments was to find a Higgs boson (it was succesfully achieved in 2012 [18]) and also there are some universal aims such as explore the physics on TeV scale, searches for undiscovered particles or extra dimensions. The main difference between CMS and ATLAS is the arrangement of magnet used for bending of created charged particles. Because this thesis deals with ATLAS experiment, it will be described it little bit closer.

ATLAS (see Fig. 1.6) a is cylinder-shape detector 46 m long and 25 m in diameter. It is placed 100 m below the ground and it weighs around 7×10^6 kg. It consists of many layers of forward-backward symmetric sub-detectors. Right-handed coordinate system is used. The z axis is identical with beam line, $x - y$ plane is perpendicular to it and x points in to center of LHC (see Fig. **??**). To easily describe each detector position (or track position of particle traveling

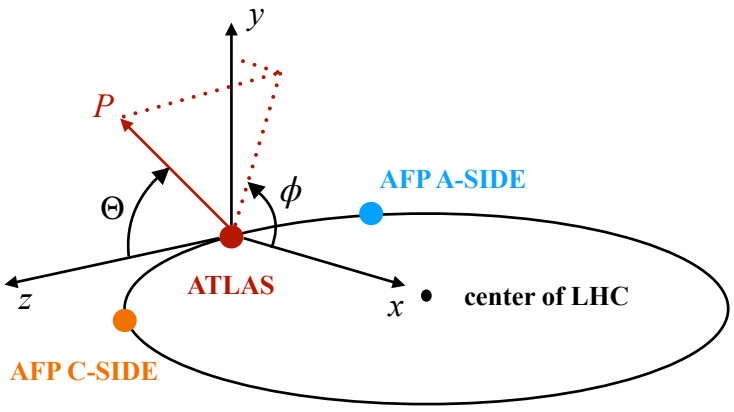

Figure 1.4: ATLAS coordinate system.

though the detector), several variables need to be defined. The angle between beam axis and measured point is denoted as Θ and azimutal angle is indicated with ϕ. Then pseudorapidity η is defined as

$$\eta = -\ln \tan \frac{\Theta}{2} = \frac{1}{2} \ln \frac{1 + \cos \Theta}{1 - \cos \Theta}. \tag{1.4}$$

When velocity of particle is relativistic, one benefits from defining the rapidity y as

$$y = \frac{1}{2} \ln \frac{E + p_z}{E - p_z} = \frac{1}{2} \ln \frac{1 + \beta \cos \Theta}{1 - \beta \cos \Theta}, \tag{1.5}$$

these two become asymptotically similar as $\beta = |\vec{v}|/c \to 1$.

Two magnet systems bend the tracks of charged particles in detector, because one can calculate the momentum of particle simply from Eq. 1.2 knowing its charge, radius of circular path and strength of external magnetic field applied to it. Central Solenoid Magnet is $5.3\ \mathrm{m}$ long, $2.4\ \mathrm{m}$ in diameter and $4.5\ \mathrm{cm}$ thick. It weight of $5\ \mathrm{t}$. It lies between Inner detector and Electromagnetic Calorimeter describe later. Its working temperature $4\ \mathrm{K}$ is achieved by cooling it with liquid Helium. There is also thick aluminium shield around, to protect it from heat. Magnetic field strength is $2\ \mathrm{T}$. Torodial magnetic field in ATLAS is created by three gigantic magnets namely Barrel Toroid and two End-cap Toroids (See Fig. 1.5). The Barrel has 8 separate coils. Length of each is $25.3\ \mathrm{m}$, its outer diameter is $20.1\ \mathrm{m}$ and weight is $830\ \mathrm{t}$. It is also cooled to $4.7\ \mathrm{K}$, producing a $4\ \mathrm{T}$ magnetic field necessary for muon spectrometer also discussed in following sections. Finally the End-cap Toroid has axial length of $5\ \mathrm{m}$, its outer diameter is $10.7\ \mathrm{m}$. One is placed at the end of each central solenoid base with weight of $240\ \mathrm{t}$ each.

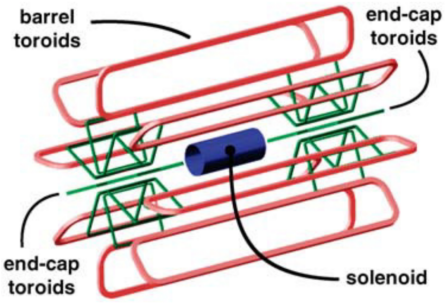

Figure 1.5: Scheme of ATLAS magnets [19]

1.3.1 Inner Detector

When a particle is produced Inner Detectror (ID) is first part of detector interacting with it [20]. Because of this fact it has to withstand high raditional doses. There are three layers of ID namely Pixel Detector, Semiconductor Tracker (SCT) and Transition Radiation Tracker (TRT) arranged as concentric cylinders around the beam axis. It covers pseudorapidity in range $|\eta| < 2.5$ of full azimutal angle ϕ. Pixel Detector contain 3 layers of pixels working in temperature around $260\ \mathrm{K}$. There are 80 million pixels (80 million channels) with size $50 \times 400\ \mu\mathrm{m}^2$ so total area is nearly $2\ \mathrm{m}^2$ [21]. If charged particle crosses the depletion region of pixel sensor, it creates a current impulse. This serves an information about, where particle hit the detector. SCT is formed of four layers and nine end-cap regions (on each side of barrel) consisting of $4,088$ microstrip tracker sensors. Those $80\ \mu\mathrm{m} \times 12\ \mathrm{cm}$ sized stripes are perpendicular to its next layer, so stripes arranged in one direction give first coordinate and next layer gives the second one. This result in total area of $60\ \mathrm{m}^2$. Strips have a same purpose as pixels in Pixel Detector.

The outermost part of ID is TRT (Transition Radiation Tracker). Each straw tube has diameter $4\ \mathrm{mm}$ and is $144\ \mathrm{cm}$ long, if straw is in barrel region ($50,000$ pieces in total), or $37\ \mathrm{cm}$ long, if it is situated in end-cap region ($250,000$ pieces in total). There is $30\ \mu\mathrm{m}$ diameter gold-plated tungsten wire inside each straw. Charged particle going thought straw ionizes a gas inside and creates electors drifting towards the wire, where it induces a signal. Straws are filled with Xenon and CO_2 [22]. There are foils interleaved between the straws. When charged particle crosses two materials with different index of refraction it produces a light signal, that could be measured. TRT helps to discriminate between electrons and charged pions.

1.3.2 Calorimeter

When particle (except muons and neutrinos) passes through calorimeter, it losses all of its energy. This energy is absorbed and measured by calorimeter. There are two types of processes causing particle to loose its energy in material - electomagnetic showering and hadron showering. For this reason there are two types of calorimeters in ATLAS detector. They both are sampling calorimeters, it means that they are made of layers of absorbing (high-density) material, interleaved with layers of an active scintillating medium, where the showering occurs.

The electromagnetic calorimeter (EM) is $6.4\ \mathrm{m}$ long and $53\ \mathrm{cm}$ thin barrel. Lead and stailess steel are absorbing materials and liquid argon is the active material [23]. Barrel region delivers information about particles with $|\eta| < 2.5$ and end-cap in range between $2.5 < |\eta| < 3$. Hadronic calorimeter consist of Tile Calorimeter (TileCal) and Liquid argon Hadronic end-cap Calorimeter (HEC) [24]. First one uses steel as abosorbing material and plastic scintilating tiles as an active material. EM has one barrel covering $|\eta| < 1$ and two end-caps in $0.8 < |\eta| < 1.7$ region. Second one is build of copper plates with liquid argon active material and it is composed of two wheels. Each wheel is segmented into two layers with the pseudorapidity coverage $1.5 < |\eta| < 3.2$.

1.3.3 Muon Spectrometer

The very last layer of ATLAS detector is Muon Spectrometer. Since muons penetrate through material much easier than other particles, one has to build dedicated detector to measure its properties. It consists of around $4,000$ chambers [25]. Muon spectrometer is composed of four types of detectors. Monitored drift tubes (MDT) are filled with mixture of argon and CO_2, in center of each tube is tungsten-rhoenuim wire [26]. Goal of MDT is to measure momentum of muons. Thin Gap Chambers are multi-wire proportional chambers placed in end-cap region. They are for triggering and second coordinate measurement. Resistive plate chambers (RPC) have two parallel plates with gap of $2\ \mathrm{mm}$, where the mixture of gas (mainly $C_2H_2F_4$) is locarted. RPC measures the p_T of muons.

Cathode Strip chambers (CSC) is similar to MDT it is just more precise (resolution of MDT is around $80\ \mu\mathrm{m}$ and $60\ \mu\mathrm{m}$ for CSC). It is situated at very end of the whole detector. Whole Muon Spectrometer is designed to measure in $|\eta| < 2.7$ region. Tubes occur in barrel also as in end-cap region.

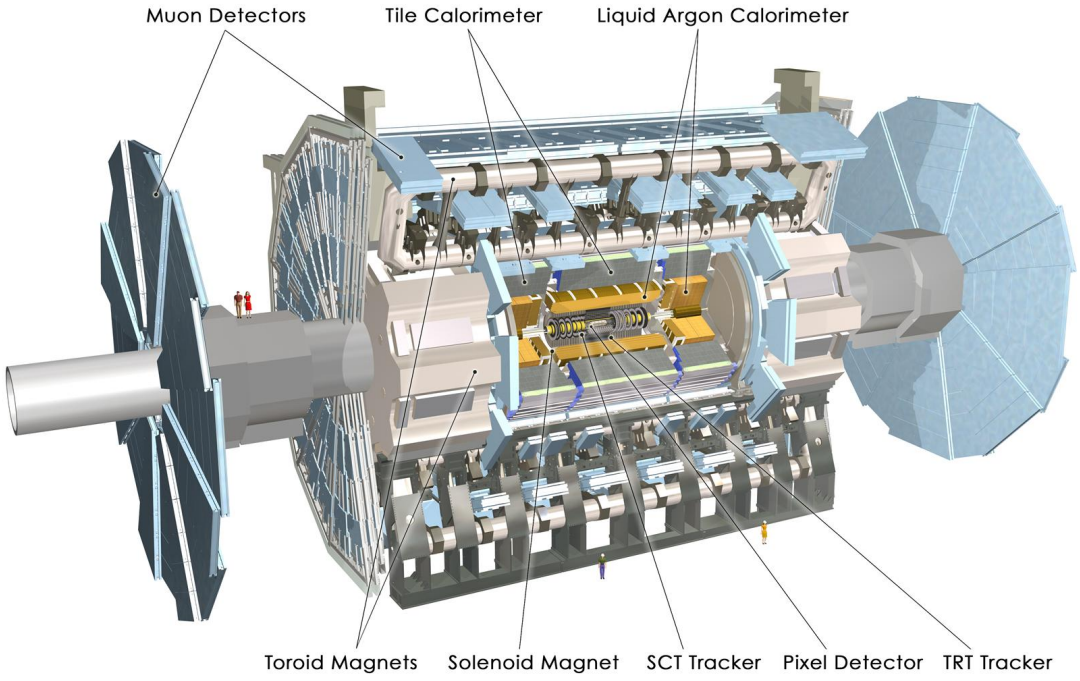

Figure 1.6: Scheme of the whole ATLAS detector. Taken from [27].

1.3.4 Forward detectors

All previously mentioned detector systems (pictured on Fig. 1.6)are called the central detector. There are also so-called forward detector systems, that measure in high $|\eta|$ ranges. LUCID (Luminosity measurement using Cherenkov Integrating Detector) is placed $17\ \mathrm{m}$ symmetrically around IP. It is Cherenkov radiation detector composed of alluminium tubes filled with C_4F_{10} gas [28]. As its name implies, it measures luminosity based on detection of innelastic part of collisions. It covers $5.5 < |\eta| < 5.9$ region. ALFA (Absolute Luminosity For ATLAS) also serves information about luminosity delivered in ATLAS IP [29]. It is placed $\pm 140\ \mathrm{m}$ away from IP, in movable devices named Roman Pots (will be discussed closer in following chapter). ALFA detector itself is composed of scintilating fibres. There is another ATLAS forward detector called AFP.

1.3.5 ATLAS Trigger

The ATLAS has an enormous frequency of colliding bunches. Because of complexity of the detector an usual event has a data size of $2\ \mathrm{MB}$ **??**. Because one bunch crosses another one in IP 4×10^7 times per second, it is crucial to save only interesting events. Interesting processes are usually rare. This implies that majority of events are trowed away, while only small portion is kept for further analysis. There are three levels of trigger deciding, if an event worth storing. Level 1 trigger (L1) is hardware based. It takes simplified information from calorimeter and Muon Spectormeter [30]. Then (few μs later) decides, if the event is interesting. Level 2 trigger (L2) is software based system that takes more detailed information from detectors and from L1. After tens of ms decides, if an event is interesting or not. Event step is last level of trigger and is also as L2 software based.

CHAPTER 2

Physics motivation

Most of interactions at LHC is ruled by strong interaction described by QCD (Quantum choromodynamics) theory. Gluons are intermediating particles for strong interaction. They are mass-less. Their most interesting property is self-interaction. Photon (intermediating particle for electromagnetic field) do not carry a charge, so it could not interact with another photon. Unlike the gluons with strong charge - colour. Another extraordinary property of strong interaction is confinement of quarks. This property is very different with comparison to electromagnetic force, where the strength of force caused by two electrically charged objects becomes weaker, when charges are further away. QCD proves that two colour charges (eg. $q\overline{q}$) being separated with energy higher than a treshold, then two another colour charged objects are produced. This means that all physically observed particles have no colour charge, even if the constituents do have.

There are several types of interaction, that could be classified according to change of four-momenta of both particles. Elastic scattering is the type of process, where initial state particles are the same as the final state ones, while they only exchange some four-momentum ($\mathbf{p_a} + \mathbf{p_b} \rightarrow \mathbf{p_a^{'}} + \mathbf{p_b^{'}}$). The inelastic scattering occurs, if the energy of particles was used for creation of new particles. Innelastic scattering, where the exchange of color-less and strongly interacting object takes place (e.g. pomeron) is called diffraction.

There are three main types of diffraction (see **??**). If one proton participating in the diffraction process brakes up and the other one survives (could be possibly measured) [31]. It is identified as single dissociation process or more often single diffraction ($\mathbf{p_a} + \mathbf{p_b} \rightarrow \mathbf{p_a^{'}} + \mathbf{p_X}$). If both protons dissociate into a higher mass, multi-particle state, process is called double diffraction ($\mathbf{p_a} + \mathbf{p_b} \rightarrow \mathbf{p_X} + \mathbf{p_Y}$). In case, that both protons remain intact and new particles are produced then we name it central exclusive production ($\mathbf{p_a} + \mathbf{p_b} \rightarrow \mathbf{p_a^{'}} + \mathbf{p_Y} + \mathbf{p_X}$).

Interesting property of diffraction are rapidity gaps. When particle interact and it is not destroyed, its path is slightly tilted (in orders of μm). This means that particle pseudorapidity will be high. Produced particles has a low pseudorapidity. Since these are well separated by the wide η region, where particles are not produced. This empty space in pseudorapidity is denoted as rapidity gap [32]. Significant problem is the fact that particle detectors are never able

to cover whole solid angle around IP. When diffractive protons stay intact, they are scattered with small angle and majority of them goes back into beam pipe. The order of mediating particle energy separate the soft diffraction and hard diffraction. The small momentum transfer between initial protons comes with difficulty - pertubative calculus could not be applied. Since most of collisions on LHC are soft-like, physics community is interested in this topic. In case of hard processes is situation much easier. Pertubation theory is suitable for these hard-scale processes.

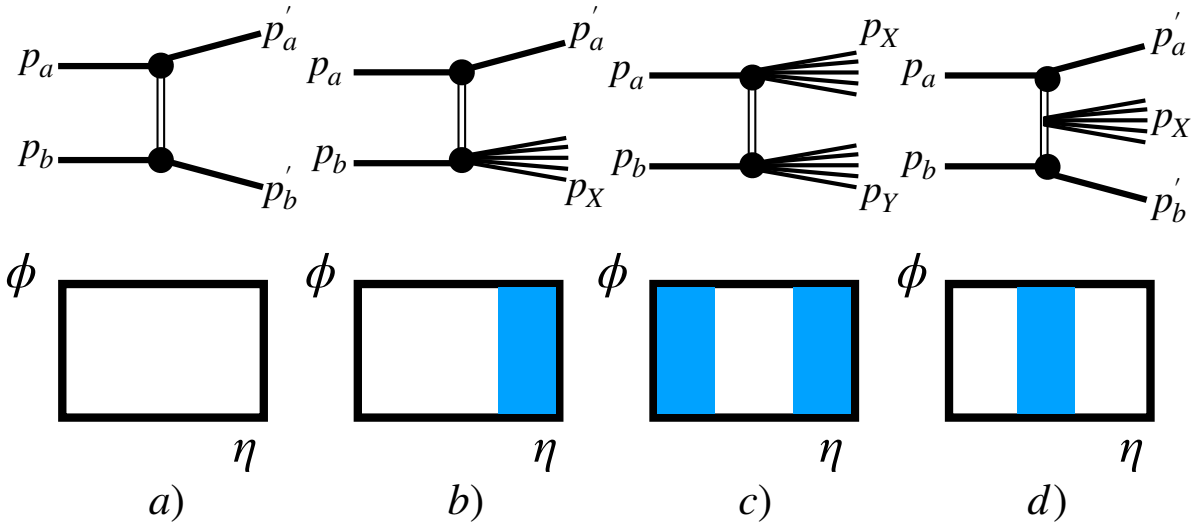

Figure 2.1: Illustration of diffractive processes with ϕ-η plane showing, what part of central detector is bombarded by created particles: a) elastic scattering, b) single diffractive process, c) double diffractive proces, d) central exclusive production.

Chapter 3

AFP

A purpose of the AFP is to measure diffractive protons emitted form a central detector in very forward direction. A protons with the small energy loss are scattered in very small angle with respect to the beam. Those protons remain in the beampipe, but could be separated from the beam. How well is the proton separated from the beam depends on portion of energy it lost also as on an emission angle at the IP. A detector capable to measure the protons has to be placed inside the beampipe [33]. It is crucial to place such a detector in to the space, where there is the only dipole magnetic field. This position is served by the space between Q5 and Q6 quadrupole (See Fig 3.1).

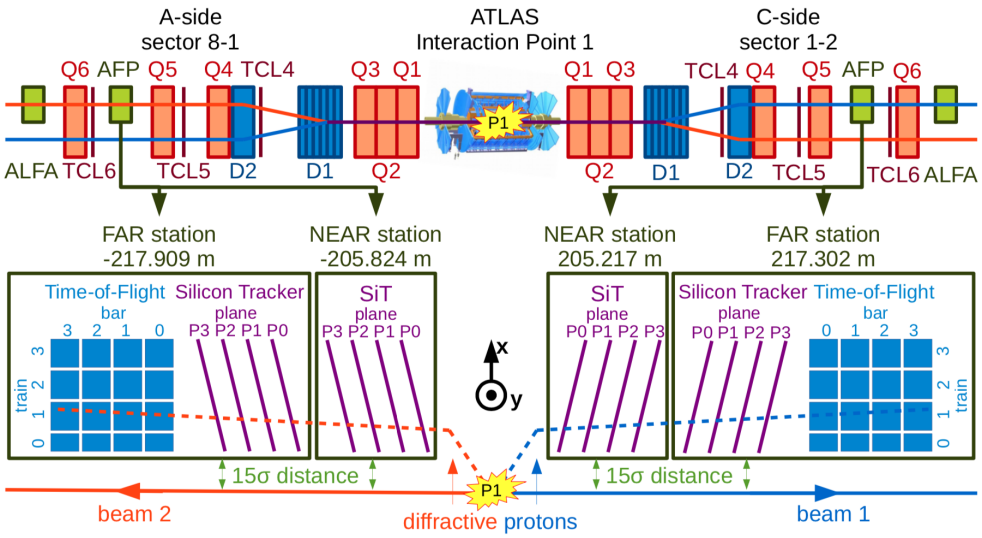

Figure 3.1: Schematic picture showing position of AFP detector. Dipole magnets D1 and D2 curving the path of protons in x direction. Quadrupole magnets Q1-Q6 focusing the beam before and after both stations of AFP detector in one side. Colimators TCL4-TCL6 protecting the quadrupole magnets from destroying. Both arms of ALFA detector at the edge of sheme could be seen. AFP setup is shown below. Tilted planes of Silicon Tracker detector together with bars of ToF detector in FAR stations [34].

The AFP (same as CMS CT-PPS) was born from FP220 and FP440 projects. It was proposed to house them in so-called Hamburg beampipe [35]. If they had some problems (RF losses and heating of device) it was decided to place the detector into movable device called the Roman Pot (discussed later). Installation of the AFP detector had a several phases. In the first one only a single-arm AFP (0+2) was placed at side C ($-z$). Two stations (just tracking sensors without Time-of-Flight detector) were placed at $206\ \mathrm{m}$ and $214\ \mathrm{m}$ far from the ATLAS IP. It measured single-diffractive events in low luminosity runs in 2016. In the second phase another arm in side A (+z) was placed symmetrically around the IP during the winter shut-down in 2017. In its final configuration the AFP detector consist of four stations (See Fig. 3.1). Each arm has two units, $NEAR$ (closer to IP) contain only the tracking sensor and FAR (furter from IP) houses the tracking sensor and the ToF (Time-of-Flight) Cherenkov timing detector.

3.1 Silicon Tracker

There is four planes of the 3D silicon pixel sensors in each station. An each sensor has 336×80 pixels and each one has a size of the $50 \times 250\ \mu\mathrm{m}$. The spatial resolution is $\sigma_x = 6\mu\mathrm{m}$ and $\sigma_y = 30\mu\mathrm{m}$. The each silicon plane is tilted 14° with respect to x axis to improve the precision in x direction. The read-out is done by the FE-I4 chip developed for the IBL project. The chip operates with a 40 MHz externally supplied clock. The requirements on silicon tracker was to sustain a enormous radiation damage (radiation dose is higher than for the first layers of the ATLAS ID), ensure the precise spacial resolution (mainly spacial) and because the detector is put close to the beam it needs to have a very small edge (in order to maximize the light mass acceptance) [36]. If the proton is measured by both of the stations separated by $12\ \mathrm{m}$ gap in z coordinate also an elevation angle could be found.

3.2 Time-of-Flight detector

Many interactions per bunch crossing in the LHC (around 40) comes with requirement to have such a detector. An idea is to match the vertex position measured by the central detector $z_{central}$ and the vertex position from the AFP as

$$z_{AFP} = c\frac{(t_{ToF_A} - t_{ToF_C})}{2},$$

where t_{ToF_A} and t_{ToF_C} is time that takes the proton to hit the detector at side A and C respectively. The ToF has to cover whole space behind the tracker, has few picosecond timing resolution and high efficiency to reconstruct the proton. The detector is build of 16 L-shaped synthetic quartz bars positioned at the Cherenkov angle with respect to the proton flight direction [37]. It was measured that timing resolution is currently around $30\ \mathrm{ps}$.

3.3 Roman Pot

Silicon Tracker and Time-of-Flight detector (in NEAR stations) are housed inside the Roman Pot device interfering with a primary vacuum of the LHC beam. They are inserted in to the beampipe in the x direction. The pot has a cylindrical shape and is guided by a sliding mechanism with a stepping motor to move precisely along few millimeters close to the beam. There is the the vacuum ($10 - 40$ mbar) inside the Roman Pot to minimize the interactions of the protons with the gas [38]. A material of the pot, as for the many LHC beam elements, is type $316LN$ stainless steel. Because of a secondary vacuum, the electronics inside the pot needs cooling.

3.4 Proton reconstruction using AFP detector

To describe the forwardly scattered protons one benefits from defining fractional energy loss as

$$\xi = \frac{\Delta E}{E} = 1 - \frac{E_0}{E},$$

where E_0 is energy of the proton before an interaction (6.5 TeV in 2017) and E is energy of the scattered proton. Phase space, where the AFP can deliver precise momentum measurement called the acceptance has a two aspect. The geometrical acceptance is defined as the fraction of the protons with given ξ and p_T measurable in the AFP to all the scattered protons with same ξ and p_T. The simulation of this effect shows that around 80% of the protons with $0.03 < \xi < 0.1$ and $p_T < 2.5$ GeV could be detected. Some of them not reach the detector because they are too close to the beam to be detected. If they lose too much energy, they probably hit a collimator or magnet. The mass acceptance gives the probability that exclusively produced system in the central detector could be measured with dependence on the AFP detector distance to the beam.

To describe how it measures an incoming proton properties one can outline how a mass spectrometer works. The mass spectrometer measures a mass of nuclei in the following principle. Firstly an accelerated ions go through velocity selector, where only ions that fulfill the condition $|\vec{v}| = |\vec{E}|/|\vec{B}|$ can continue. When charged particle enters the magnetic field and it travels in circular path according to Eq. 1.2. It could be seen that as the mass of nuclei gets the bigger radius it follows is also bigger. So if an exact position, where it hits the detector is measured, one can deduce the mass it has.

With the AFP detector is situation little bit different. The measured particles are protons, all with the equal mass. They are selected using a collimators. So from position, where the protons hit the AFP one can deduce its velocity (momentum).

The proton surviving the interaction in IP is described according its four-momentum $\mathbf{p} = (E, p_x, p_y, p_z)$. It is assumed that it remains ultrarelativistic. This assumption enable one to approximate $E \approx p_z$, so only three unknowns in the momentum four-vector remains. Then it follows this procedure

$$\text{AFP hits} \rightarrow (x, y, z)_{AFP} \rightarrow (E, p_x, p_y, p_z)_{proton}.$$

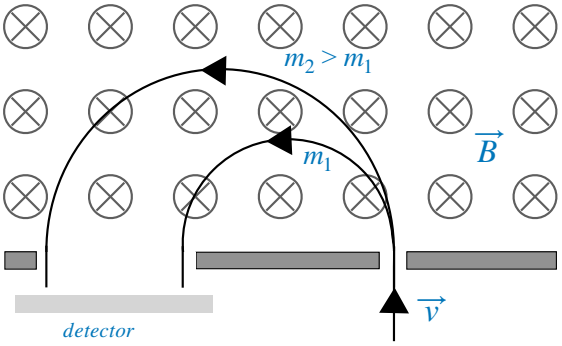

Figure 3.2: Scheme of magnetic spectrometer.

From the silicon pixel hits the clusters are created using a clustering algorithm. Usually hits in three or four planes are required. The chi-squared algorithm fit is performed to connect a clusters and forms a track. From the track coordinates the momentum four-vector of the proton is calculated. When the proton loses more energy (ξ is bigger) the distance between its path and the beam is bigger. The energy loss has bigger impact on x coordinate, since it is predominant direction of steering done by dipoles D1 and D2. According to this fact it was fount that one-to-one quadratic function

$$x(\xi) = -119\xi - 164\xi^2$$

describes the position of the proton in the FAR stations with uncertainty of $20\ \mu\mathrm{m}$ and uncertainty of $150\ \mu\mathrm{m}$ for the $NEAR$ stations. For this reason is a precision in x coordinate crucial aspect of the detector. For inversion of this formula one can obtain ξ. A non-zero crossing angle affects y coordinate. Changes in p_x and p_y induce changes in x and y coordinates respectively. So for given ξ the spread in $x - y$ plane arise from non-zero p_T.

CHAPTER 4

Alignment Methods

The AFP detector measures the protons scattered into small angles using spacial measurement. An exact position of the detector have to by known. The AFP detector parts are inserted and retracted into the LHC beampipe and for the each data-taking period is their position different. When the beam is not stable at the start of the run, the detectors are in their home positions and later they are placed close to the beam. To be able to compare the data measured in a different time period one should develop a data-driven alignment methods to be sure, where the parts of the AFP detector were placed. The alignment could be studied only if strength of the magnets is precisely known, because the magnetic field bends them. The wrong alignment also leads to the wrong assumption on the detector acceptance. The position of each part of the detector depends on the many different aspects. The position of the beam centre is extracted using BPM (Beam Position Monitoring) systems. The precision of the motor in the RP inserting the detector into the beampipe is also important (slight vibrations and temperature fluctuations cause deformations). These effets affect a global alignment of the detector. If the global alignment is perfect, the track with ξ reconstructed by AFP is same as ξ of the proton emitted at the vertex. Plus there could be so-called local misalignment, resulting from a tilt of planes in $x - y$, $x - z$ or $y - z$ planes or from non-equidistant placement of planes.

4.0.1 In situ dimuon alignment method

This global alignment method takes exclusive dimuon events, where track from the AFP is correlated with a system of muons. From the energy of muons one can find a $\xi_{\mu\mu}$ of the proton that created them. Hence the position, where the proton should hit the AFP detetor. If one subtract a difference between $\xi_{\mu\mu}$ and ξ_{AFP} for many events, the peak at $\xi_{\mu\mu} - \xi_{AFP} = 0$ should appear. Because of the imperfections in alignment, the mean value of the peak is not exactly at 0, but the slight displacement could be seen. So the peak is fitted by the Gaussian distribution and distance of mean from 0 is interpreted as a misalignment. This method assumes that muon properties are correct.

Method found that misalignment is $0.340\ \mathrm{mm}$ for station 0, $0.280\ \mathrm{mm}$ for station 1, $0.170\ \mathrm{mm}$ for station 2 and $0.360\ \mathrm{mm}$ for station 3. The systematic uncertainty relies on resolution of the peak and is found to be around $300\ \mu\mathrm{m}$.

4.0.2 Local interplane alignment method

This local alignment method uses the positions of clusters in the each plane to measure rotation of the plane with the respect to the other planes. For each plane in the station there are three possible rotations and three possible offsets. Currently the method is able to predict offsets in x and y also as rotation about z axis only. How these misalignment parameters could be derived will be described now. At the start we assume that detector is perfectly aligned. The tracks are reconstructed and only the tracks with zero slope are selected. For the each selected track is required to have a cluster in the three or four planes in one station. It is also required to have only one cluster per plane. After the track is reconstructed, the difference between cluster hits and the final track is calculated. The residuals are fitted and from these alignment parameters are extracted. Then the alignment parameters are updated with new ones and procedure is repeated. True position of the track is given by $\vec{r_t} = (x, y, z)^T$ and the measured track position $\vec{r_m} = M\vec{r_t} + \delta\vec{r}$ is acknowledged by rotation matrix and linear offset $\delta\vec{r}$ where rotation matrix is

$$M = \begin{pmatrix} 1 & \alpha & \beta \\ \alpha & 1 & \text{-}\gamma \\ \text{-}\beta & \gamma & 1 \end{pmatrix},$$

then the misalignment could be obtained as $\vec{r_m} - \vec{r_t}$. The alignment is found with respect to station 0. This method found the misalignment is $137.91\ \mu\mathrm{m}$ for station 1, $-51.25\ \mu\mathrm{m}$ and $-79.20\ \mu\mathrm{m}$. The ATLAS Standard Model Bootstrap Generator tool was used to find the statistic uncertainties with result less than $1\ \mu\mathrm{m}$ for all the stations. A systematic uncertainties have not been found yet.

CHAPTER 5

Hot-spot alignment method

The hot-spot global alignment method was used first in alignment studies in the ALFA forward detector. Then it was studied on the MC (Monte Carlo) samples for the AFP detector [39], where it was shown that this method is very promising. The principle of the Hot-spot method is to find the bottleneck of the transverse hit distribution and use its position as reference point. This Hot-spot position is then compared to position gathered the from simulation and the difference between those gives the offset of the detector. The advantage of this method is that it provides the information about an alignment to the every station independently to others. The another interesting fact is that it uses the diffractive scattered protons and since the cross section for this process is large, there is such a big statistic that could be used. It also has a small sensitivity to the physics model and the optics changes and it is not dependent on the central detector as the In situ alignment method discussed in previous chapter.

The data used for presented analysis were collected in the special BBA (Beam Based Alignment) run in 2017. This special run number 324195 happened at night between $21 - 22/05/2017$ and more information about this run could be found at the ATLAS run query webpage. To find the exact position of the detector, one have to find a positions of the beam centre and the RP. The position of the RP in this specific run could be seen on Fig. 5.1 and Tab. 5.1.

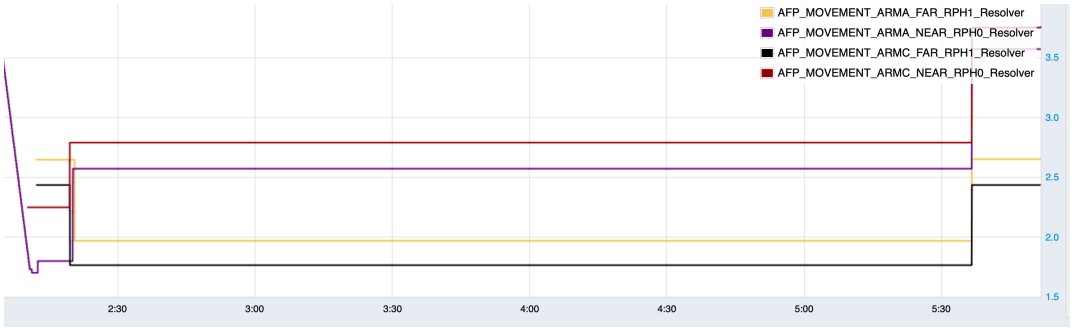

Figure 5.1: Position of RP in run 324195. Could be find on ATLAS DDV webpage.

	NEAR [mm]	FAR [mm]
ARM A	0.864	1.045
ARM C	1.155	0.891

Table 5.1: Position of beam centre from AFP twiki webpage.

From Fig. 5.1 it could be seen that from $2:30$ to $5:30$ were pots in the stable position and hence it is a perfect time to perform this study. This time period corresponds to $350-423$ lumiblock range used in this analysis. Then the expected position of the first AFP pixel could be calculated using values from Tab. 5.1 and Tab. 5.2.

	NEAR [mm]	FAR [mm]
ARM A	2.57	1.97
ARM C	2.79	1.77

Table 5.2: Position of RP in run 324195 from Fig. 5.1.

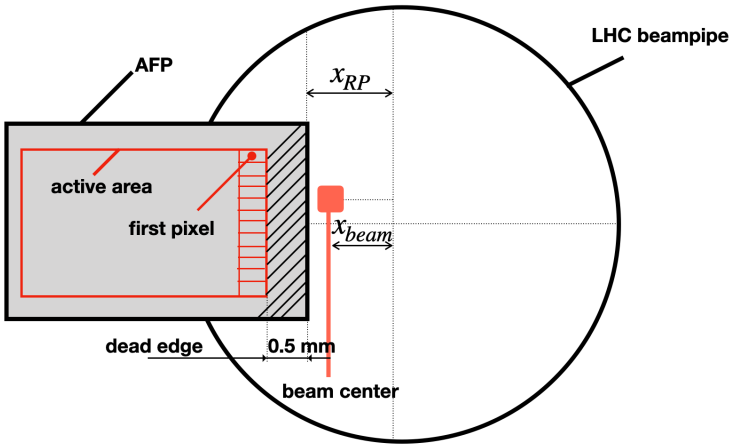

Figure 5.2: Scheme of AFP detector.

From Fig. 5.2 it could be seen that the position of the detector is defined as

$$X = x_{RP} + 0.5 - x_{beam} \tag{5.1}$$

where x_{beam} is the position of the beam from Tab. 5.1, x_{RP} is the position of the RP from Tab. 5.2 plus one have to add 0.5 mm for the detector dead edge. This finally gives the position of each station in Tab. 5.3 below.

	NEAR [mm]	FAR [mm]
ARM A	2.206	1.425
ARM C	2.135	1.379

Table 5.3: Position of AFP detector in run 324195. Given by Eq. 5.1, Tab. 5.1 and 5.2.

5.1 Hot-spot position

The position of the detector could be determined using the characteristic point in the transverse hit pattern as a reference point. The distribution of $x - y$ track coordinates for all the stations could be seen on Fig. 5.11. It seems like the distributions are turned around the x axis. This is because the simulation was done for the earlier period, when the crossing angle in the central detector was different. When one turns the MC into the same direction as data the overall result is more or less same. This proves the fact that only the shape of distribution matters.

What is the best selection of tracks used for this study is the key aspect. In the first iteration only events, when there was just one track per station were used. Since this assumption did not give a consistent result for the both methods presented in the following sections (and hence a systematic uncertainty is big), it was necessary to apply the another conditions. Because of this events were restricted to those, where there was only one track in the both stations per side. This rapidly improves the results. To increase the statistics one came with another condition. If the events, where there is only one track per stations is used, one gets only 2 values for one station (one for each method). Since this is not enough, the selection on the limit of the distance between the position reconstructed by $NEAR$ and FAR detector was used. The difference between particular coordinates of the tracks from the reconstructed protons is pictured on Fig. 5.16.

It could be seen that the difference between the data and the MC is large. The significance of this disagreement is even better visible on Fig. 5.26. Not only the shape but also the portion of events that are thrown away when applying the selection cut. When one tries to match the cuts in the way that the percentage of selected events is similar, hit pattern for the MC was destroyed. This shows the indication that smearing of the MC is imperfect. The many different variations of this selection was probed. Such as make a cut just on the difference between $|y^{FAR} - y^{NEAR}|$ or $|x^{FAR} - x^{NEAR}|$. This case successfully cleaned the $NEAR$ stations, but for the FAR ones this was unacceptable. Also circular condition $|y^{FAR} - y^{NEAR}|^2 + |x^{FAR} - x^{NEAR}|^2$ was studied, but there was no such improvement, when compared to $|y^{FAR} - y^{NEAR}| + |x^{FAR} - x^{NEAR}|$ cut used in the further analysis.

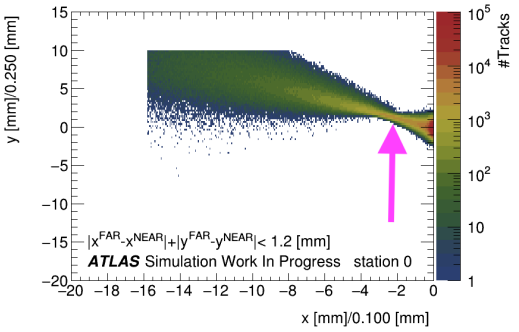

a) MC station 0

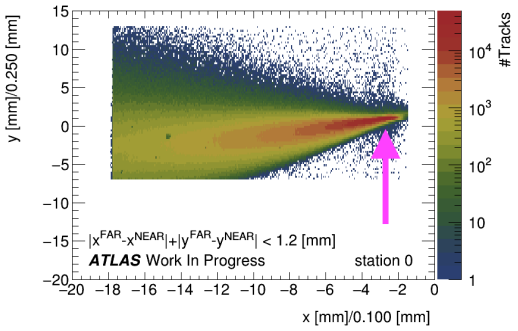

b) data station 0

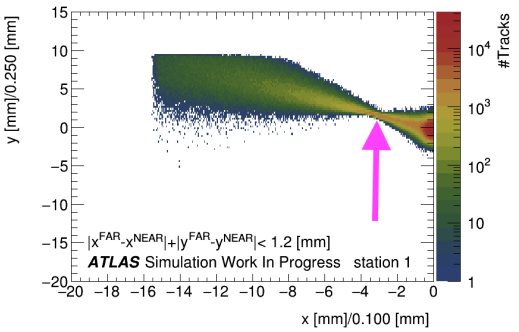

c) MC station 1

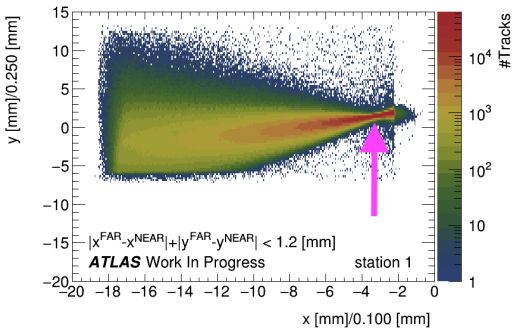

d) data station 1

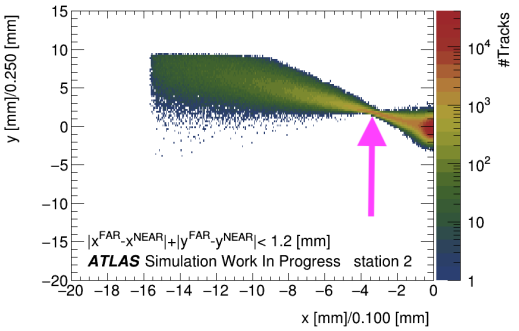

e) MC station 2

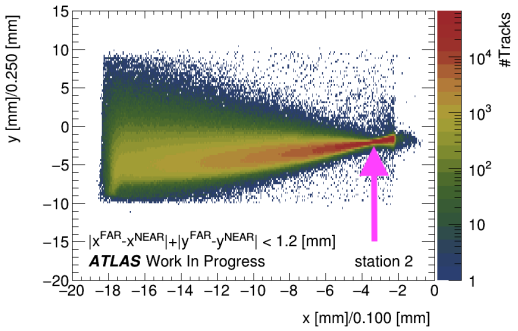

f) data station 2

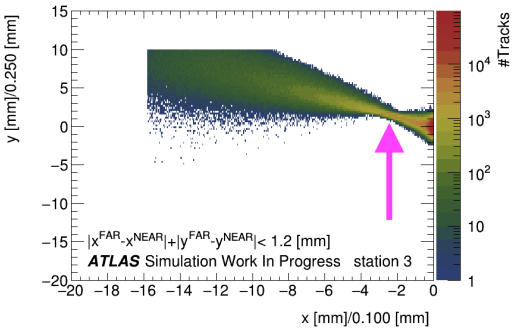

g) MC station 3

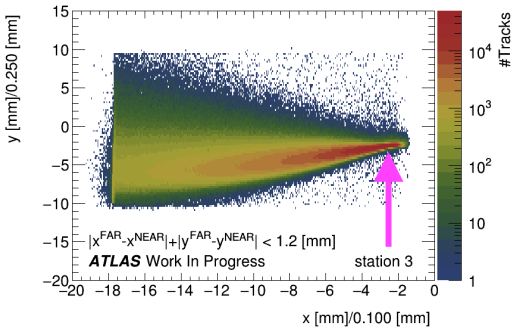

h) data station 3

Figure 5.11: Transverse hit pattern in all stations for data and MC. Pink arrow points to predicted position of the Hot-spot. Difference direction of the distribution is caused by non corresponding crossing angle.

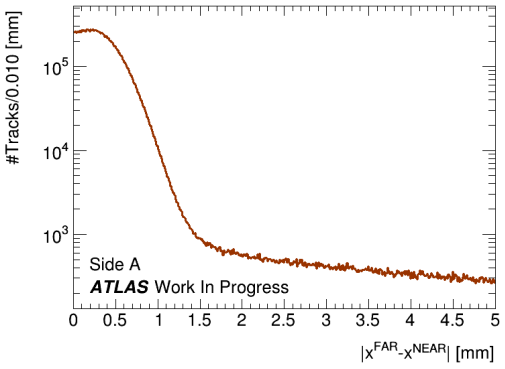

a) x coordinate side A for data

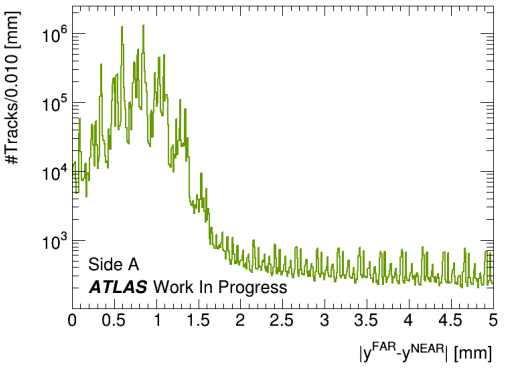

b) y coordinate side A for data

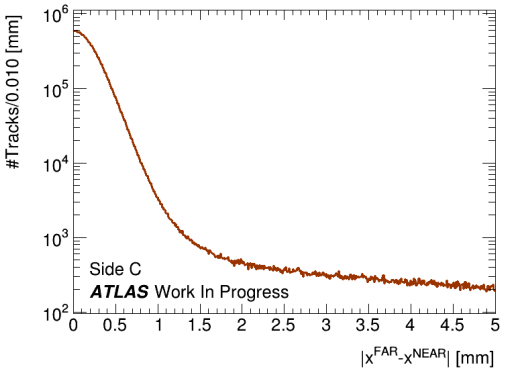

c) x coordinate side C for data

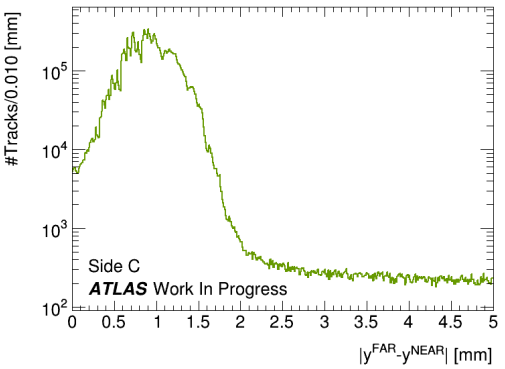

d) y coordinate side C for data

Figure 5.16: Difference between positions of track simulated for side A (station 0 and station 1) and side C (station station 2 and station 3).

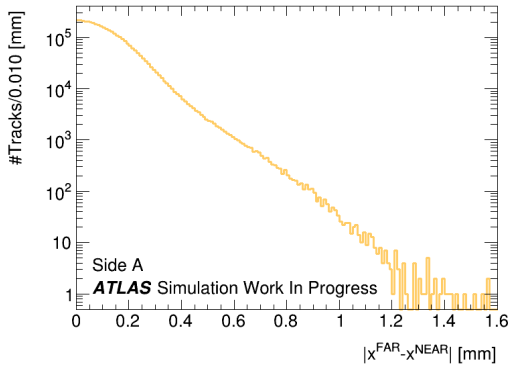

a) x coordinate side A for MC

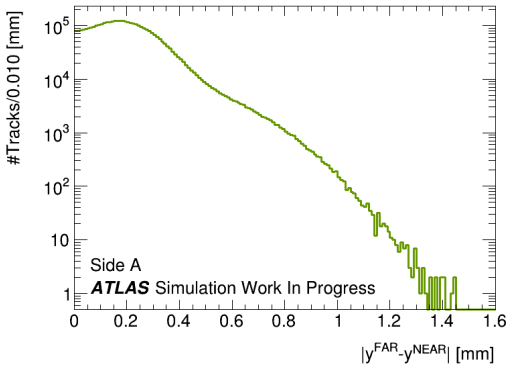

b) y coordinate side A for MC

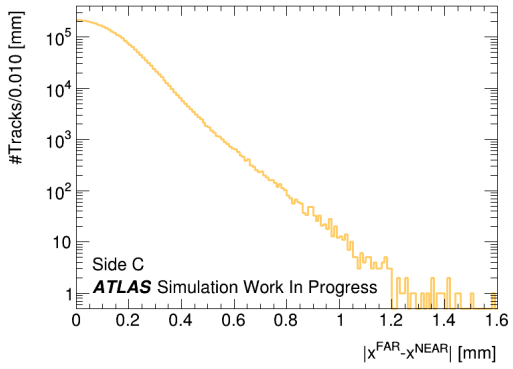

c) x coordinate side C for MC

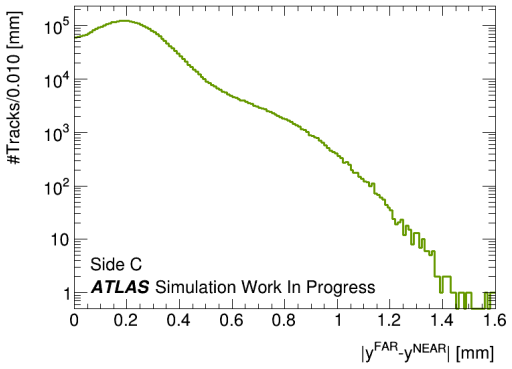

d) y coordinate side C for MC

Figure 5.21: Difference between positions of track reconstructed in one event between in $NEAR$ and FAR stations for one coordinate on MC.

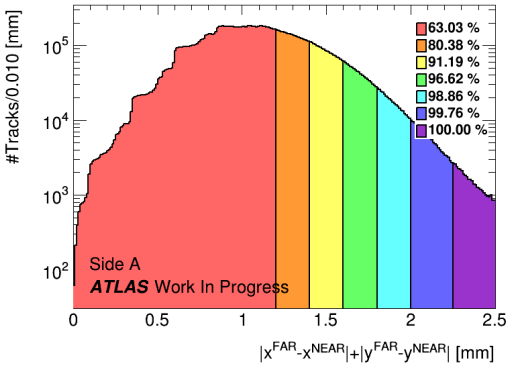

a) side A for data

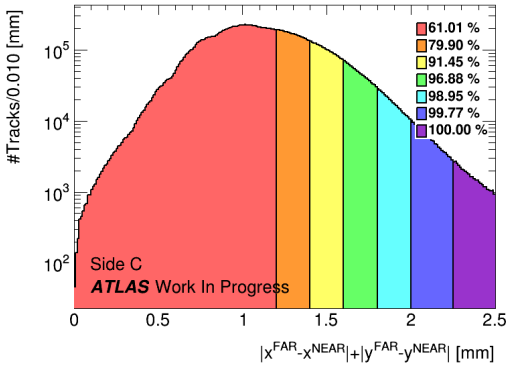

b) side C for data

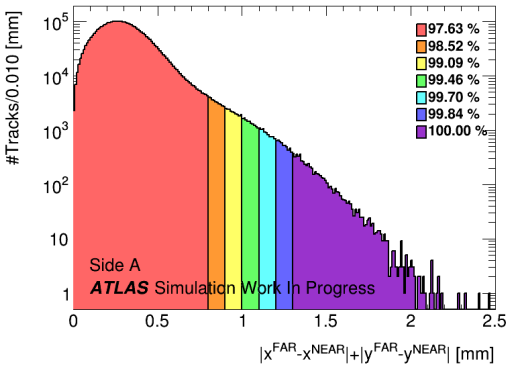

c) side A for MC

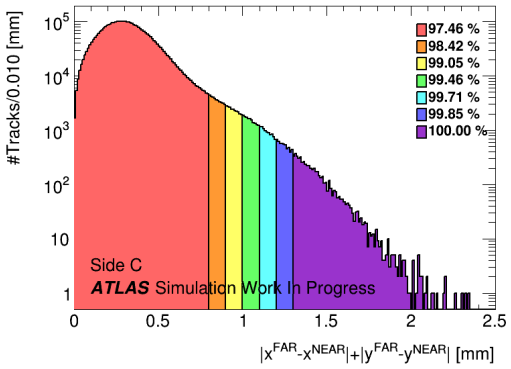

d) side C for MC

Figure 5.26: Distribution of the differences between both track coordinates for side A (station 0 and 1) and for side C (station 1 and 2). The percentage in legend of the plot correspond to percentage of the tracks passing the selection. For example in Fig. 5.26 a) it says that 1.60 selection keeps 91.19 % of the tracks.

5.2 TProfile method

This method calculates the Hot-spot position using the standard deviation of the distribution. Its name comes from the class in the ROOT framework, that calculates the standard deviation of the given data and was used before, when the unbinned data was used. For the each bin size in x coordinate (x slice) is the standard deviation of y track positions calculated. The standard deviation gives the dispersion of values. This values are printed in the TProfile histogram. Parabolic fit in the $\pm\ 0.5\ \mathrm{mm}$ range from the expected position of the Hot-spot is performed. Instead of the regular quadratic function $ax^2 + bx + c$, where the all parameters are uncorrelated is special form used. The fitting function is

$$A(x - B)^2 + C, \tag{5.2}$$

so instead of extracting vertex of parabola from the regular expression $-b/(2a)$ is the middle of parabola just value of the fitting parameter B. The new parabolic fit in $B \pm 0.5\ \mathrm{mm}$ range is performed. The same function as for the first fit is used. The position of the Hot-spot is taken as value of the parameter B given by the second fit. Statistic uncertainty is error of B estimated by ROOT. Results for the TProfile method in all used bin sizes and selection are in Tab. B.1 and Tab. B.3.

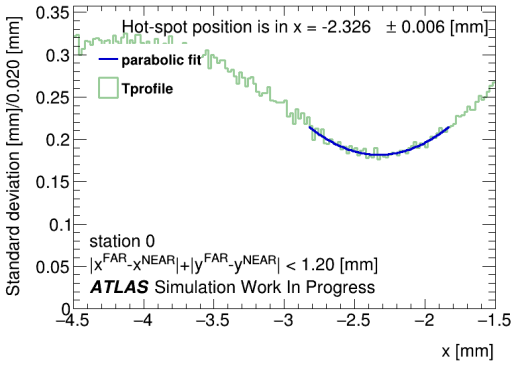

a) MC station 0

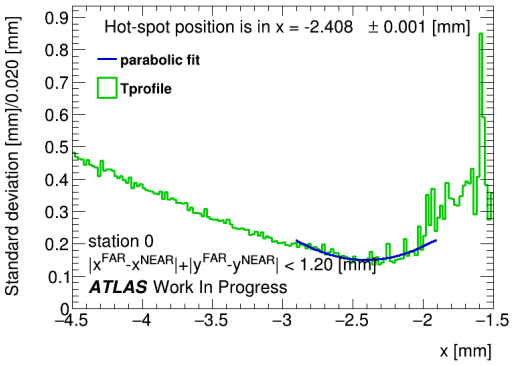

b) data station 0

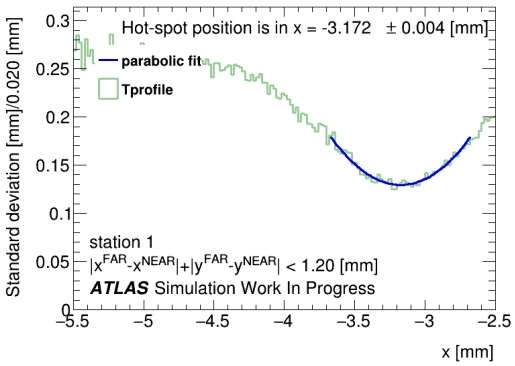

b) MC station 1

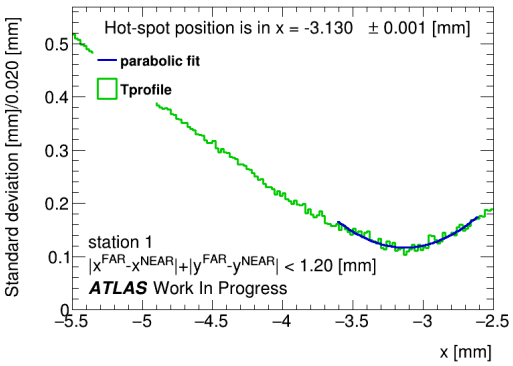

c) data station 1

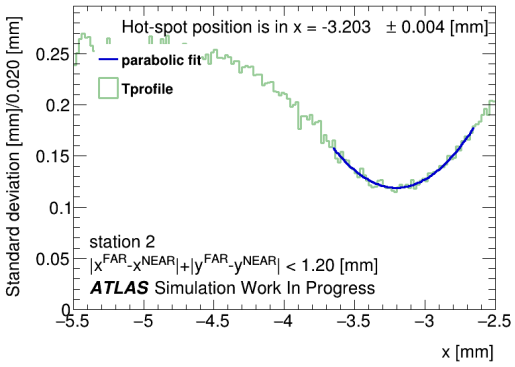

d) MC station 2

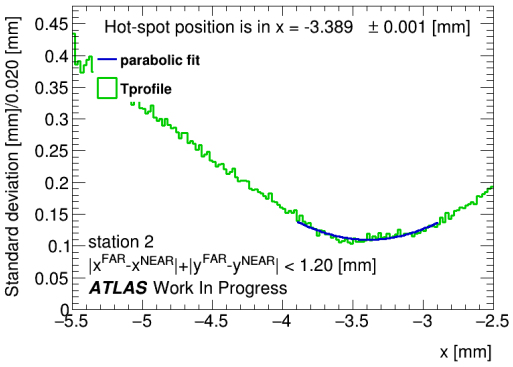

e) data station 2

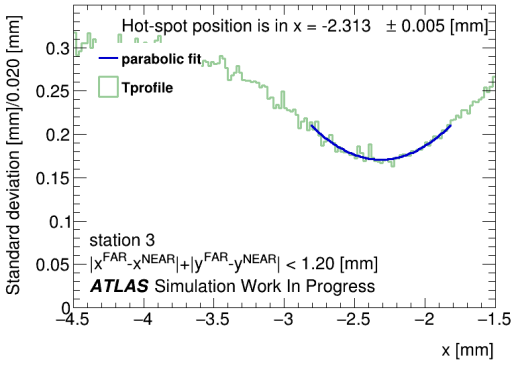

f) MC station 3

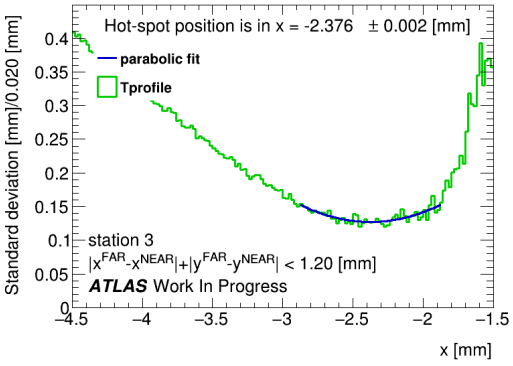

f) data station 3

Figure 5.35: TProfile histogram for $|y^{FAR} - y^{NEAR}| + |x^{FAR} - x^{NEAR}| < 1.2$ [mm] performed on data and MC. Bin in x has a size of 0.020 mm.

5.3 FitSlices method

This method calculates the width of the distribution in slight different way. When the tracks are classified into the selections, hit pattern is sliced according to x bin size chosen. Each x bin is then fitted using Gaussian distribution and its width is extracted. As it was shown in [39] the width is highly dependent on the y bin size. Generally the larger bin size of y is better. But it was found that $250\ \mu\mathrm{m}$ is the best option. But this was not enough.

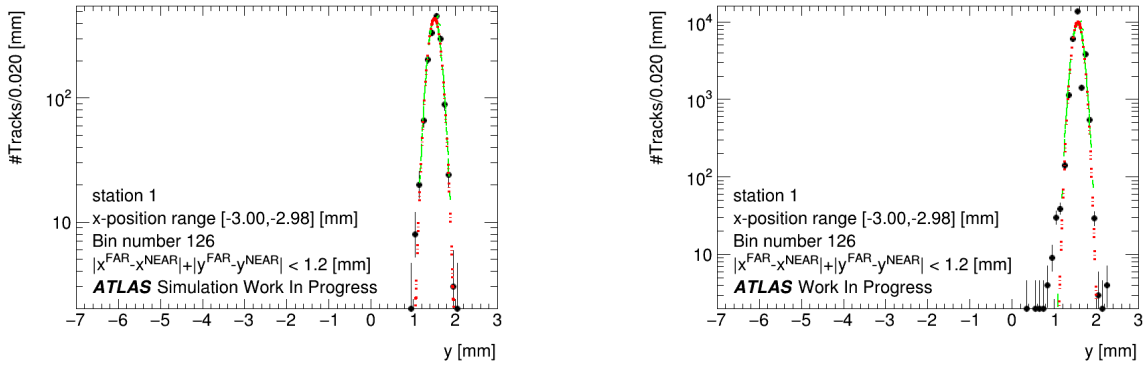

a) MC a) data

Figure 5.38: Slice of x bin number 126 (corresponding to x-position range [-3.00,-2.98] [mm]) for 1.2 selection. Dash-dotted green line is the first gaussian and green dash-dotted line is the function of second fit result for MC a) and data b).

Because of this fact unbinned case was studied. It turned out that this gives the much consistent results than for the binned histogram. So the unbinned y distribution was used in the further analysis. To get an idea of the method see Fig. 5.38. The fit by gauss function in full range of the plot is performed. Then the another gaussian fit is done $\pm\ 0.5\ \mathrm{mm}$ around mean of the first gauss. The width of second gaussian and its error is filled in FitSlices histogram. Afterwards the procedure is the same as for TProfile method. Two parabolic fits with function 5.2 is done (see Fig. 5.47). The results are for this method are in Tab. B.5 and Tab. B.7.

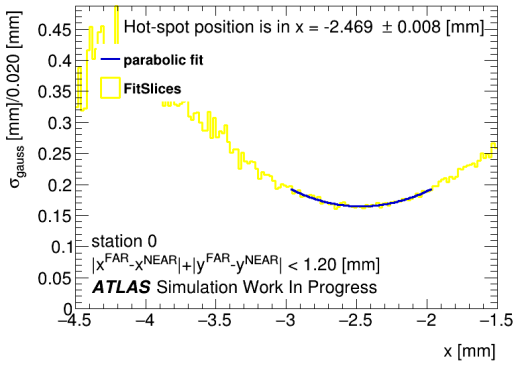

a) MC station 0

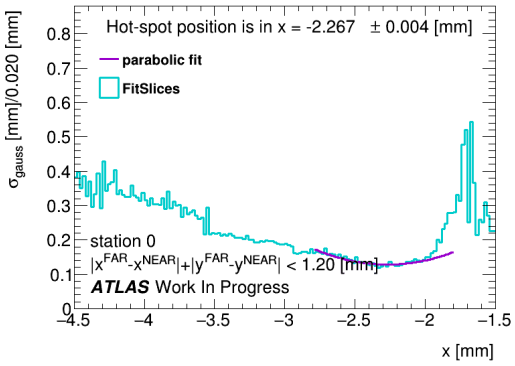

b) data station 0

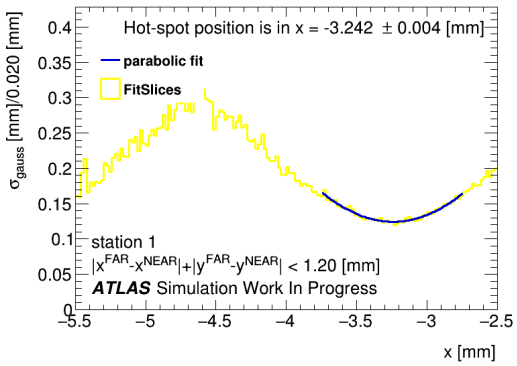

c) MC station 1

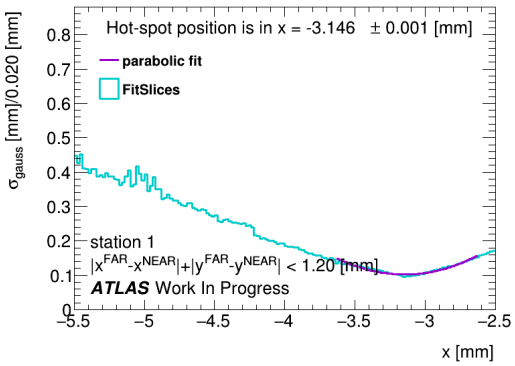

c) data station 1

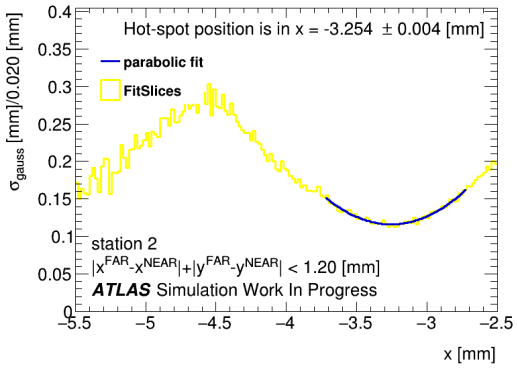

e) MC station 2

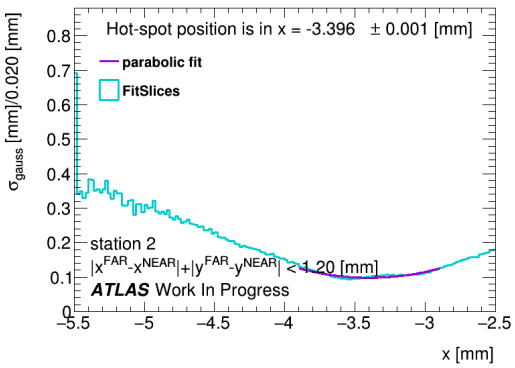

f) data station 2

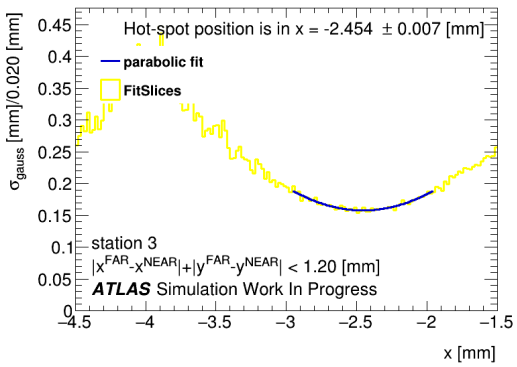

g) MC station 3

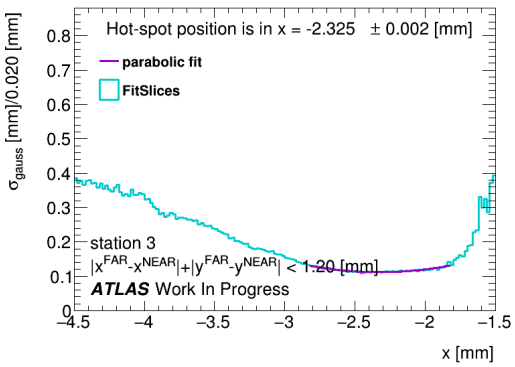

h) data station 3

Figure 5.47: Histograms for FitSlices method performed on MC and data with $|y^{FAR} - y^{NEAR}| + |x^{FAR} - x^{NEAR}| < 1.2$ [mm] selection. Bin in x has a size of 0.020 mm.

5.4 Results

After Hot-spot positions were calculated for all bin widths for the both TProfile and FitSlices method. The same estimation of the final Hot-spot position was performed on MC and data. Averages were obtained for each bin size. Error is the maximum value of errors for different bins. TProfile method results in MC for station 0, station 1, station 2 and station 3 in Tab. A.2, Tab. B.2, Tab. C.2 and Tab. D.2 respectively and for data in A.4, Tab. B.4, Tab. C.4 and Tab. D.4 respectively. FitSlices method results on MC are in Tab. A.6, Tab. B.6, Tab. C.6 and Tab. D.6 for station 0, station 1, station 2 and station 3 respectively and for data in A.8, Tab. B.8, Tab. C.4 and Tab. D.8 respectively.

5.5 Exact position of AFP detector

Finally after all previous steps, the position and its corrections to the position of all stations the detector was found. For each station and each method the differences between the MC and the data was obtained (absolute value of the difference). This gives 7 values for each method and each station. For one station all differences were calculated between each selection and each method. For one station this gives 196 differences of Hot-spot position estimation an average value of those was found and this was taken as the offset of the detector (see Tab. A.9, Tab. B.9, Tab. C.9 and Tab. D.9). Systematic uncertainty is standard deviation of all of those differences. The results of performed study are in Tab. 5.4.

	correction [mm]
station 0	0.122 ± 0.059 (syst.) $\pm$ 0.008 (stat.)
station 1	0.079 ± 0.049 (syst.) $\pm$ 0.004 (stat.)
station 2	0.071 ± 0.055 (syst.) $\pm$ 0.004 (stat.)
station 3	0.117 ± 0.079 (syst.) $\pm$ 0.007 (stat.)

Table 5.4: Correction for precise alignment for each station. Systematic error is standard deviation of the differences between data and MC. Statistical error is the maximum of fit parameter errors given by ROOT.

Summary

The AFP detector could provide an extension to the physics studied on LHC. This forward detector consisting of four stations all placed more than $200\ \mathrm{m}$ away from the center of the ATLAS detector is in operation since 2016. The FAR stations (being more far from interaction point) consist of silicon pixel tracker and the Time-of-Flight detector. The $NEAR$ stations house only tracker. At this moment the Time-of-Flight detector is not used in standard analyses because it needs to collect both protons participating in interaction.

Scattered protons that hit the AFP detector form a cluster and if one interlink the clusters from two or more planes, it gives a track of incoming proton. When optic of the LHC is known, the spacial coordinates of the track can be related to four-momentum of the incoming proton. Because the predominant direction of the D1 and D2 (dipoles placed between interaction point and AFP detector) is x, the precision in x is much more essential than the one in y-direction. While y coordinate of the track is related to transverse momentum p_T of the proton, one could find the relation between fractional energy loss ξ and X distance from the beam. This one-to-one mapping was found by the AFP collaboration.

Precision in x therefore gives precision of reconstructed proton proton properties so its precision is crucial to all analyses using AFP detector. There are some methods that estimate the position, this could be divided into global and local one. In situ dimuon alignment method rely on precision of reconstruction muons produced in central detector. Local interplane alignment method can only give the offset of the station with respect to other. Hot-spot alignment method has none of defects mentioned above. It finds the characteristic position of the track spacial distribution (bottleneck) and compare its position with simulation.

Hot-spot alignment method was performed on data form special beam based alignment run 324195 from 2017 in this work. Many different variations of this method were studied in more detail. Two methods of finding the Hot-spot position independently were tuned. The TProfile method calculates the width of the distribution using standard deviation of slice in x with given bin size. The FitSlices method cut the distribution into the slices and fit its unbinned data with the Gaussian distribution and width is extracted. Corrections to AFP positions were calculated

for all stations of AFP detector using both methods. The result of this study is in Tab. 5.4. The corrections are in order of tens of $\mu\mathrm{m}$. This result shows that the optics is well-understood. Achieved result will lead to the reduction of systematic uncertainty related to AFP measurements and thus will improve results in all related analyses.

APPENDIX A

Station 0

bin width	0.010 [mm]	0.015 [mm]	0.020 [mm]	0.025 [mm]	0.050 [mm]
sel. 0.8	-2.406 ± 0.006	-2.405 ± 0.005	-2.407 ± 0.006	-2.406 ± 0.006	-2.406 ± 0.006
sel. 0.9	-2.372 ± 0.006	-2.373 ± 0.005	-2.373 ± 0.006	-2.372 ± 0.006	-2.372 ± 0.006
sel. 1.0	-2.349 ± 0.006	-2.348 ± 0.006	-2.349 ± 0.006	-2.348 ± 0.006	-2.348 ± 0.006
sel. 1.1	-2.331 ± 0.006	-2.331 ± 0.006	-2.331 ± 0.006	-2.330 ± 0.006	-2.332 ± 0.006
sel. 1.2	-2.324 ± 0.006	-2.326 ± 0.006	-2.326 ± 0.006	-2.324 ± 0.006	-2.325 ± 0.006
sel. 1.3	-2.324 ± 0.006	-2.326 ± 0.006	-2.326 ± 0.006	-2.323 ± 0.006	-2.325 ± 0.006
sel. 2.5	-2.324 ± 0.006	-2.324 ± 0.006	-2.324 ± 0.006	-2.322 ± 0.006	-2.325 ± 0.006

Table A.1: The result of TProfile method on MC from station 0.

sel. 0.8	-2.406 ± 0.006
sel. 0.9	-2.372 ± 0.006
sel. 1.0	-2.348 ± 0.006
sel. 1.1	-2.331 ± 0.006
sel. 1.2	-2.325 ± 0.006
sel. 1.3	-2.325 ± 0.006
sel. 2.5	-2.324 ± 0.006

Table A.2: Average over bin sizes for TProfile method on MC for station 0.

bin width	0.010 [mm]	0.015 [mm]	0.020 [mm]	0.025 [mm]	0.050 [mm]
sel. 1.20	-2.402 ± 0.001	-2.409 ± 0.001	-2.408 ± 0.001	-2.412 ± 0.001	-2.414 ± 0.001
sel. 1.40	-2.404 ± 0.001	-2.407 ± 0.001	-2.407 ± 0.001	-2.409 ± 0.001	-2.409 ± 0.001
sel. 1.60	-2.430 ± 0.001	-2.432 ± 0.001	-2.430 ± 0.001	-2.434 ± 0.001	-2.430 ± 0.001
sel. 1.80	-2.456 ± 0.001	-2.457 ± 0.001	-2.457 ± 0.001	-2.460 ± 0.001	-2.458 ± 0.001
sel. 2.00	-2.479 ± 0.001	-2.480 ± 0.001	-2.480 ± 0.001	-2.482 ± 0.001	-2.475 ± 0.001
sel. 2.25	-2.508 ± 0.001	-2.509 ± 0.001	-2.510 ± 0.001	-2.510 ± 0.001	-2.507 ± 0.001
sel. 2.50	-2.528 ± 0.001	-2.531 ± 0.001	-2.529 ± 0.001	-2.529 ± 0.001	-2.527 ± 0.001

Table A.3: The result of TProfile method on data from station 0.

sel. 1.20	-2.409 ± 0.001
sel. 1.40	-2.407 ± 0.001
sel. 1.60	-2.431 ± 0.001
sel. 1.80	-2.458 ± 0.001
sel. 2.00	-2.479 ± 0.001
sel. 2.25	-2.509 ± 0.001
sel. 2.50	-2.529 ± 0.001

Table A.4: Average over bin sizes for TProfile method on data for station 0.

bin width	0.010 [mm]	0.015 [mm]	0.020 [mm]	0.025 [mm]	0.050 [mm]
sel. 0.8	-2.492 ± 0.007	-2.492 ± 0.007	-2.491 ± 0.007	-2.492 ± 0.007	-2.492 ± 0.007
sel. 0.9	-2.482 ± 0.007	-2.481 ± 0.007	-2.481 ± 0.007	-2.482 ± 0.008	-2.484 ± 0.007
sel. 1.0	-2.472 ± 0.008	-2.473 ± 0.008	-2.473 ± 0.008	-2.473 ± 0.008	-2.472 ± 0.008
sel. 1.1	-2.467 ± 0.008	-2.467 ± 0.008	-2.470 ± 0.008	-2.470 ± 0.008	-2.469 ± 0.008
sel. 1.2	-2.466 ± 0.008	-2.465 ± 0.008	-2.469 ± 0.008	-2.469 ± 0.008	-2.468 ± 0.008
sel. 1.3	-2.466 ± 0.008	-2.466 ± 0.008	-2.469 ± 0.008	-2.468 ± 0.008	-2.468 ± 0.008
sel. 2.5	-2.465 ± 0.008	-2.466 ± 0.008	-2.469 ± 0.008	-2.468 ± 0.008	-2.468 ± 0.008

Table A.5: The result of FitSlices method on MC from station 0.

sel. 0.8	-2.492 ± 0.007
sel. 0.9	-2.482 ± 0.008
sel. 1.0	-2.473 ± 0.008
sel. 1.1	-2.469 ± 0.008
sel. 1.2	-2.467 ± 0.008
sel. 1.3	-2.467 ± 0.008
sel. 2.5	-2.467 ± 0.008

Table A.6: Weighted average over bin sizes for FitSlices method on MC for station 0.

bin width	0.010 [mm]	0.015 [mm]	0.020 [mm]	0.025 [mm]	0.050 [mm]
sel. 1.20	-2.273 ± 0.003	-2.268 ± 0.004	-2.267 ± 0.004	-2.264 ± 0.004	-2.299 ± 0.002
sel. 1.40	-2.331 ± 0.002	-2.332 ± 0.002	-2.336 ± 0.002	-2.331 ± 0.002	-2.333 ± 0.002
sel. 1.60	-2.349 ± 0.002	-2.350 ± 0.002	-2.357 ± 0.002	-2.351 ± 0.002	-2.351 ± 0.002
sel. 1.80	-2.355 ± 0.002	-2.355 ± 0.002	-2.359 ± 0.002	-2.356 ± 0.002	-2.357 ± 0.002
sel. 2.00	-2.358 ± 0.002	-2.359 ± 0.002	-2.360 ± 0.002	-2.360 ± 0.002	-2.355 ± 0.002
sel. 2.25	-2.360 ± 0.002	-2.361 ± 0.002	-2.361 ± 0.002	-2.363 ± 0.002	-2.358 ± 0.002
sel. 2.50	-2.363 ± 0.002	-2.362 ± 0.002	-2.363 ± 0.002	-2.362 ± 0.002	-2.361 ± 0.002

Table A.7: The result of FitSlices method on data from station 0.

sel. 1.20	-2.274 $\pm$ 0.002
sel. 1.40	-2.333 $\pm$ 0.002
sel. 1.60	-2.352 $\pm$ 0.002
sel. 1.80	-2.356 $\pm$ 0.002
sel. 2.00	-2.358 $\pm$ 0.002
sel. 2.25	-2.361 $\pm$ 0.002
sel. 2.50	-2.361 $\pm$ 0.002

Table A.8: Average over bin sizes for FitSlices method on data for station 0.

selection		1.20	1.40	1.60	1.80	2.00	2.25	2.50	1.20	1.40	1.60	1.80	2.00	2.25	2.50
	result	-2.409	-2.407	-2.431	-2.458	-2.479	-2.509	-2.529	-2.274	-2.333	-2.352	-2.356	-2.358	-2.361	-2.361
0.8	-2.406	0.003	0.001	0.025	0.052	0.073	0.103	0.123	0.132	0.073	0.054	0.050	0.048	0.045	0.045
0.9	-2.372	0.037	0.035	0.059	0.086	0.107	0.137	0.157	0.098	0.039	0.020	0.016	0.014	0.011	0.011
1.0	-2.348	0.061	0.059	0.083	0.110	0.131	0.161	0.181	0.074	0.015	0.004	0.008	0.010	0.013	0.013
1.1	-2.331	0.078	0.076	0.100	0.127	0.148	0.178	0.198	0.057	0.002	0.021	0.025	0.027	0.030	0.030
1.2	-2.325	0.084	0.082	0.106	0.133	0.154	0.184	0.204	0.051	0.008	0.027	0.031	0.033	0.036	0.036
1.3	-2.325	0.084	0.082	0.106	0.133	0.154	0.184	0.204	0.051	0.008	0.027	0.031	0.033	0.036	0.036
2.5	-2.324	0.085	0.083	0.107	0.134	0.155	0.185	0.205	0.050	0.009	0.028	0.132	0.034	0.037	0.037
0.8	-2.492	0.083	0.085	0.061	0.034	0.013	0.017	0.037	0.218	0.159	0.140	0.136	0.134	0.131	0.131
0.9	-2.482	0.073	0.075	0.051	0.024	0.003	0.027	0.047	0.208	0.149	0.130	0.126	0.124	0.121	0.121
1.0	-2.473	0.064	0.066	0.042	0.015	0.006	0.036	0.056	0.199	0.140	0.121	0.117	0.115	0.112	0.112
1.1	-2.469	0.060	0.062	0.038	0.011	0.010	0.040	0.060	0.195	0.136	0.117	0.113	0.111	0.108	0.108
1.2	-2.467	0.058	0.060	0.036	0.009	0.012	0.042	0.062	0.193	0.134	0.115	0.111	0.109	0.106	0.106
1.3	-2.467	0.058	0.060	0.036	0.009	0.012	0.042	0.062	0.193	0.134	0.115	0.111	0.109	0.106	0.106
2.5	-2.467	0.058	0.060	0.036	0.009	0.012	0.042	0.062	0.193	0.134	0.115	0.111	0.109	0.106	0.106

Table A.9: Diffrences between data and MC for station 0.

APPENDIX B

Station 1

bin width	0.010 [mm]	0.015 [mm]	0.020 [mm]	0.025 [mm]	0.050 [mm]
sel. 0.8	-3.229 ± 0.003	-3.228 ± 0.003	-3.228 ± 0.003	-3.228 ± 0.003	-3.228 ± 0.003
sel. 0.9	-3.210 ± 0.003	-3.209 ± 0.004	-3.208 ± 0.003	-3.209 ± 0.003	-3.208 ± 0.003
sel. 1.0	-3.194 ± 0.003	-3.194 ± 0.003	-3.194 ± 0.004	-3.193 ± 0.003	-3.194 ± 0.004
sel. 1.1	-3.179 ± 0.003	-3.179 ± 0.003	-3.178 ± 0.003	-3.177 ± 0.003	-3.181 ± 0.004
sel. 1.2	-3.173 ± 0.004	-3.173 ± 0.004	-3.172 ± 0.004	-3.171 ± 0.004	-3.176 ± 0.004
sel. 1.3	-3.168 ± 0.004	-3.169 ± 0.004	-3.168 ± 0.004	-3.167 ± 0.004	-3.169 ± 0.004
sel. 2.5	-3.167 ± 0.004	-3.168 ± 0.004	-3.167 ± 0.004	-3.166 ± 0.004	-3.167 ± 0.004

Table B.1: The result of TProfile method on MC from station 1.

sel. 0.8	-3.228 ± 0.001
sel. 0.9	-3.209 ± 0.002
sel. 1.0	-3.194 ± 0.002
sel. 1.1	-3.179 ± 0.002
sel. 1.2	-3.173 ± 0.002
sel. 1.3	-3.168 ± 0.002
sel. 2.5	-3.167 ± 0.002

Table B.2: Average over bin sizes for TProfile method on MC for station 1.

bin width	0.010 [mm]	0.015 [mm]	0.020 [mm]	0.025 [mm]	0.050 [mm]
sel. 1.20	-3.130 ± 0.001	-3.133 ± 0.001	-3.130 ± 0.001	-3.130 ± 0.001	-3.129 ± 0.001
sel. 1.40	-3.128 ± 0.001	-3.130 ± 0.001	-3.129 ± 0.001	-3.129 ± 0.001	-3.127 ± 0.001
sel. 1.60	-3.122 ± 0.001	-3.123 ± 0.001	-3.123 ± 0.001	-3.121 ± 0.001	-3.121 ± 0.001
sel. 1.80	-3.107 ± 0.001	-3.108 ± 0.001	-3.109 ± 0.001	-3.108 ± 0.001	-3.109 ± 0.001
sel. 2.00	-3.095 ± 0.001	-3.098 ± 0.001	-3.095 ± 0.001	-3.096 ± 0.001	-3.099 ± 0.001
sel. 2.25	-3.074 ± 0.001	-3.075 ± 0.001	-3.074 ± 0.001	-3.076 ± 0.001	-3.075 ± 0.001
sel. 2.50	-3.059 ± 0.001	-3.059 ± 0.001	-3.059 ± 0.001	-3.058 ± 0.001	-3.06 ± 0.001

Table B.3: The results of TProfile method on data from station 1.

sel. 1.20	-3.130 ± 0.001
sel. 1.40	-3.129 ± 0.001
sel. 1.60	-3.122 ± 0.001
sel. 1.80	-3.108 ± 0.001
sel. 2.00	-3.097 ± 0.001
sel. 2.25	-3.075 ± 0.001
sel. 2.50	-3.059 ± 0.001

Table B.4: Average over bin sizes for TProfile method on data for station 1.

bin width	0.010 [mm]	0.015 [mm]	0.020 [mm]	0.025 [mm]	0.050 [mm]
sel. 0.8	-3.241 ± 0.004	-3.241 ± 0.004	-3.241 ± 0.004	-3.240 ± 0.004	-3.241 ± 0.004
sel. 0.9	-3.237 ± 0.004	-3.238 ± 0.004	-3.237 ± 0.004	-3.238 ± 0.004	-3.240 ± 0.004
sel. 1.0	-3.244 ± 0.004	-3.245 ± 0.004	-3.244 ± 0.004	-3.243 ± 0.004	-3.244 ± 0.004
sel. 1.1	-3.242 ± 0.004	-3.242 ± 0.004	-3.241 ± 0.004	-3.243 ± 0.004	-3.244 ± 0.004
sel. 1.2	-3.246 ± 0.004	-3.246 ± 0.004	-3.242 ± 0.004	-3.244 ± 0.004	-3.245 ± 0.004
sel. 1.3	-3.244 ± 0.004	-3.245 ± 0.004	-3.242 ± 0.004	-3.244 ± 0.004	-3.244 ± 0.004
sel. 2.5	-3.244 ± 0.004	-3.242 ± 0.004	-3.241 ± 0.004	-3.243 ± 0.004	-3.244 ± 0.004

Table B.5: The result of FitSlices method on MC from station 1.

sel. 0.8	-3.241 ± 0.004
sel. 0.9	-3.238 ± 0.004
sel. 1.0	-3.244 ± 0.004
sel. 1.1	-3.242 ± 0.004
sel. 1.2	-3.245 ± 0.004
sel. 1.3	-3.244 ± 0.004
sel. 2.5	-3.243 ± 0.004

Table B.6: Average over bin sizes for FitSlices method on MC for station 1.

sel. 1.20	-3.148 ± 0.001	-3.148 ± 0.001	-3.146 ± 0.001	-3.148 ± 0.001	-3.151 ± 0.001
sel. 1.40	-3.176 ± 0.001	-3.176 ± 0.001	-3.177 ± 0.001	-3.178 ± 0.001	-3.176 ± 0.001
sel. 1.60	-3.192 ± 0.001	-3.193 ± 0.001	-3.194 ± 0.001	-3.193 ± 0.001	-3.196 ± 0.001
sel. 1.80	-3.194 ± 0.001	-3.195 ± 0.001	-3.196 ± 0.001	-3.195 ± 0.001	-3.198 ± 0.001
sel. 2.00	-3.194 ± 0.001	-3.195 ± 0.001	-3.195 ± 0.001	-3.195 ± 0.001	-3.198 ± 0.001
sel. 2.25	-3.193 ± 0.001	-3.193 ± 0.001	-3.194 ± 0.001	-3.194 ± 0.001	-3.197 ± 0.001
sel. 2.50	-3.193 ± 0.001	-3.194 ± 0.001	-3.194 ± 0.001	-3.194 ± 0.001	-3.197 ± 0.001

Table B.7: The result of FitSlices method on data from station 1.

sel. 1.20	-3.148 ± 0.001
sel. 1.40	-3.177 ± 0.001
sel. 1.60	-3.194 ± 0.001
sel. 1.80	-3.196 ± 0.001
sel. 2.00	-3.195 ± 0.001
sel. 2.25	-3.194 ± 0.001
sel. 2.50	-3.194 ± 0.001

Table B.8: Weighted average over bin sizes for FitSlices method on data for station 1.

selection		1.20	1.40	1.60	1.80	2.00	2.25	2.50	1.20	1.40	1.60	1.80	2.00	2.25	2.50
	result	-3.130	-3.129	-3.122	-3.108	-3.097	-3.075	-3.059	-3.148	-3.177	-3.194	-3.196	-3.195	-3.194	-3.194
0.8	-3.228	0.098	0.099	0.106	0.120	0.131	0.153	0.169	0.080	0.051	0.034	0.032	0.033	0.034	0.034
0.9	-3.209	0.079	0.080	0.087	0.101	0.112	0.134	0.150	0.061	0.032	0.015	0.013	0.014	0.015	0.015
1.0	-3.194	0.064	0.065	0.072	0.086	0.097	0.119	0.135	0.046	0.017	0.000	0.002	0.001	0.000	0.000
1.1	-3.179	0.049	0.050	0.057	0.071	0.082	0.104	0.120	0.031	0.002	0.015	0.017	0.016	0.015	0.015
1.2	-3.173	0.043	0.044	0.051	0.065	0.076	0.098	0.114	0.025	0.004	0.021	0.023	0.022	0.021	0.021
1.3	-3.168	0.038	0.039	0.046	0.060	0.071	0.093	0.109	0.020	0.009	0.026	0.028	0.027	0.026	0.026
2.5	-3.167	0.037	0.038	0.045	0.059	0.070	0.092	0.108	0.019	0.010	0.027	0.029	0.028	0.027	0.027
0.8	-3.241	0.111	0.112	0.119	0.133	0.144	0.166	0.182	0.093	0.064	0.047	0.045	0.046	0.047	0.047
0.9	-3.238	0.108	0.109	0.116	0.130	0.141	0.163	0.179	0.090	0.061	0.044	0.042	0.043	0.044	0.044
1.0	-3.244	0.114	0.115	0.122	0.136	0.147	0.169	0.185	0.096	0.067	0.050	0.048	0.049	0.050	0.050
1.1	-3.243	0.113	0.114	0.121	0.135	0.146	0.168	0.184	0.095	0.066	0.049	0.047	0.048	0.049	0.049
1.2	-3.245	0.115	0.116	0.123	0.137	0.148	0.170	0.186	0.097	0.068	0.051	0.049	0.050	0.051	0.051
1.3	-3.244	0.114	0.115	0.122	0.136	0.147	0.169	0.185	0.096	0.067	0.050	0.048	0.049	0.050	0.050
2.5	-3.243	0.113	0.114	0.121	0.135	0.146	0.168	0.184	0.095	0.066	0.049	0.047	0.048	0.049	0.049

Table B.9: Diffrences between data and MC for station 1.

APPENDIX C

Station 2

bin width	0.010 [mm]	0.015 [mm]	0.020 [mm]	0.025 [mm]	0.050 [mm]
sel. 0.8	-3.284 ± 0.003	-3.284 ± 0.003	-3.284 ± 0.003	-3.284 ± 0.003	-3.286 ± 0.004
sel. 0.9	-3.254 ± 0.003	-3.252 ± 0.003	-3.252 ± 0.003	-3.254 ± 0.003	-3.254 ± 0.003
sel. 1.0	-3.228 ± 0.003	-3.228 ± 0.003	-3.228 ± 0.003	-3.227 ± 0.003	-3.228 ± 0.003
sel. 1.1	-3.212 ± 0.004	-3.214 ± 0.003	-3.213 ± 0.003	-3.212 ± 0.004	-3.214 ± 0.003
sel. 1.2	-3.206 ± 0.004	-3.205 ± 0.003	-3.203 ± 0.004	-3.205 ± 0.004	-3.206 ± 0.004
sel. 1.3	-3.196 ± 0.003	-3.196 ± 0.003	-3.196 ± 0.003	-3.196 ± 0.003	-3.196 ± 0.003
sel. 2.5	-3.196 ± 0.003	-3.195 ± 0.003	-3.196 ± 0.003	-3.195 ± 0.003	-3.196 ± 0.003

Table C.1: The result of TProfile method on MC from station 2.

sel. 0.8	-3.284 ± 0.004
sel. 0.9	-3.254 ± 0.003
sel. 1.0	-3.228 ± 0.003
sel. 1.1	-3.113 ± 0.004
sel. 1.2	-3.205 ± 0.004
sel. 1.3	-3.196 ± 0.003
sel. 2.5	-3.195 ± 0.003

Table C.2: Average over bin sizes for TProfile method on MC for station 2.

bin width	0.010 [mm]	0.015 [mm]	0.020 [mm]	0.025 [mm]	0.050 [mm]
sel. 1.20	-3.390 ± 0.001	-3.389 ± 0.001	-3.389 ± 0.001	-3.389 ± 0.001	-3.390 ± 0.001
sel. 1.40	-3.323 ± 0.001	-3.325 ± 0.001	-3.326 ± 0.001	-3.323 ± 0.001	-3.322 ± 0.001
sel. 1.60	-3.266 ± 0.001	-3.268 ± 0.001	-3.268 ± 0.001	-3.266 ± 0.001	-3.269 ± 0.001
sel. 1.80	-3.234 ± 0.001	-3.230 ± 0.001	-3.231 ± 0.001	-3.230 ± 0.001	-3.227 ± 0.001
sel. 2.00	-3.209 ± 0.001	-3.207 ± 0.001	-3.206 ± 0.001	-3.205 ± 0.001	-3.205 ± 0.001
sel. 2.25	-3.186 ± 0.001	-3.186 ± 0.001	-3.188 ± 0.001	-3.184 ± 0.001	-3.184 ± 0.001
sel. 2.50	-3.179 ± 0.001	-3.173 ± 0.001	-3.176 ± 0.001	-3.173 ± 0.001	-3.173 ± 0.001

Table C.3: The result of TProfile method on data from station 2.

sel. 1.20	-3.389 ± 0.001
sel. 1.40	-3.324 ± 0.001
sel. 1.60	-3.267 ± 0.001
sel. 1.80	-3.230 ± 0.001
sel. 2.00	-3.206 ± 0.001
sel. 2.25	-3.186 ± 0.001
sel. 2.50	-3.175 ± 0.001

Table C.4: Average over bin sizes for TProfile method on data for station 2.

bin width	0.010 [mm]	0.015 [mm]	0.020 [mm]	0.025 [mm]	0.050 [mm]
sel. 0.8	-3.286 ± 0.003	-3.286 ± 0.003	-3.286 ± 0.003	-3.286 ± 0.003	-3.288 ± 0.004
sel. 0.9	-3.263 ± 0.004	-3.263 ± 0.004	-3.262 ± 0.004	-3.262 ± 0.004	-3.265 ± 0.004
sel. 1.0	-3.257 ± 0.004	-3.257 ± 0.004	-3.255 ± 0.004	-3.257 ± 0.004	-3.259 ± 0.004
sel. 1.1	-3.255 ± 0.004	-3.255 ± 0.004	-3.255 ± 0.004	-3.256 ± 0.004	-3.258 ± 0.004
sel. 1.2	-3.254 ± 0.004	-3.255 ± 0.004	-3.254 ± 0.004	-3.255 ± 0.004	-3.259 ± 0.004
sel. 1.3	-3.254 ± 0.004	-3.254 ± 0.004	-3.254 ± 0.004	-3.255 ± 0.004	-3.258 ± 0.004
sel. 2.5	-3.252 ± 0.004	-3.254 ± 0.004	-3.253 ± 0.004	-3.253 ± 0.004	-3.256 ± 0.004

Table C.5: The result of FitSlices method on MC from station 2.

sel. 0.8	-3.286 ± 0.004
sel. 0.9	-3.263 ± 0.004
sel. 1.0	-3.257 ± 0.004
sel. 1.1	-3.256 ± 0.004
sel. 1.2	-3.255 ± 0.004
sel. 1.3	-3.255 ± 0.004
sel. 2.5	-3.253 ± 0.004

Table C.6: Average over bin sizes for FitSlices method on MC for station 2.

bin width	0.010 [mm]	0.015 [mm]	0.020 [mm]	0.025 [mm]	0.050 [mm]
sel. 1.20	-3.397 ± 0.001	-3.397 ± 0.001	-3.396 ± 0.001	-3.396 ± 0.001	-3.396 ± 0.001
sel. 1.40	-3.327 ± 0.001	-3.328 ± 0.001	-3.329 ± 0.001	-3.329 ± 0.001	-3.325 ± 0.001
sel. 1.60	-3.292 ± 0.001	-3.293 ± 0.001	-3.294 ± 0.001	-3.290 ± 0.001	-3.290 ± 0.001
sel. 1.80	-3.289 ± 0.001	-3.289 ± 0.001	-3.287 ± 0.001	-3.290 ± 0.001	-3.285 ± 0.001
sel. 2.00	-3.289 ± 0.001	-3.288 ± 0.001	-3.286 ± 0.001	-3.287 ± 0.001	-3.285 ± 0.001
sel. 2.25	-3.288 ± 0.001	-3.288 ± 0.001	-3.287 ± 0.001	-3.288 ± 0.001	-3.284 ± 0.001
sel. 2.50	-3.286 ± 0.001	-3.288 ± 0.001	-3.286 ± 0.001	-3.287 ± 0.001	-3.283 ± 0.001

Table C.7: The result of FitSlices method on data from station 2.

sel. 1.20	-3.396 $\pm$ 0.001
sel. 1.40	-3.328 $\pm$ 0.001
sel. 1.60	-3.292 $\pm$ 0.001
sel. 1.80	-3.288 $\pm$ 0.001
sel. 2.00	-3.287 $\pm$ 0.001
sel. 2.25	-3.287 $\pm$ 0.001
sel. 2.50	-3.286 $\pm$ 0.001

Table C.8: Average over bin sizes for FitSlices method on data for station 2.

selection		1.20	1.40	1.60	1.80	2.00	2.25	2.50	1.20	1.40	1.60	1.80	2.00	2.25	2.50
	result	-3.389	-3.324	-3.267	-3.230	-3.206	-3.186	-3.175	-3.396	-3.328	-3.282	-3.288	-3.287	-3.287	-3.286
0.8	-3.284	0.105	0.040	0.017	0.054	0.078	0.098	0.109	0.112	0.044	0.002	0.004	0.003	0.003	0.002
0.9	-3.254	0.135	0.070	0.013	0.024	0.048	0.068	0.079	0.142	0.074	0.028	0.034	0.033	0.033	0.032
1.0	-3.228	0.161	0.096	0.039	0.002	0.022	0.042	0.053	0.168	0.100	0.054	0.060	0.059	0.059	0.058
1.1	-3.113	0.276	0.211	0.154	0.117	0.093	0.073	0.062	0.283	0.215	0.169	0.175	0.174	0.174	0.173
1.2	-3.205	0.184	0.119	0.062	0.025	0.001	0.019	0.030	0.191	0.123	0.077	0.083	0.082	0.082	0.081
1.3	-3.196	0.193	0.128	0.071	0.034	0.010	0.010	0.021	0.200	0.132	0.086	0.092	0.091	0.091	0.090
2.5	-3.195	0.194	0.129	0.072	0.035	0.011	0.009	0.020	0.201	0.133	0.087	0.093	0.092	0.092	0.091
0.8	-3.286	0.103	0.038	0.019	0.056	0.080	0.100	0.111	0.110	0.042	0.004	0.002	0.001	0.001	0.000
0.9	-3.263	0.126	0.061	0.004	0.033	0.057	0.077	0.088	0.133	0.065	0.019	0.025	0.024	0.024	0.023
1.0	-3.257	0.132	0.067	0.010	0.027	0.051	0.071	0.082	0.139	0.071	0.025	0.031	0.030	0.030	0.029
1.1	-3.256	0.133	0.068	0.011	0.026	0.050	0.070	0.081	0.140	0.072	0.026	0.032	0.031	0.031	0.030
1.2	-3.255	0.134	0.069	0.012	0.025	0.049	0.069	0.080	0.141	0.073	0.027	0.033	0.032	0.032	0.031
1.3	-3.255	0.134	0.069	0.012	0.025	0.049	0.069	0.080	0.141	0.073	0.027	0.033	0.032	0.032	0.031
2.5	-3.253	0.136	0.071	0.014	0.023	0.047	0.067	0.078	0.143	0.075	0.029	0.035	0.034	0.034	0.033

Table C.9: Diffrences between data and MC for station 2.

APPENDIX **D**

Station 3

bin width	0.010 [mm]	0.015 [mm]	0.020 [mm]	0.025 [mm]	0.050 [mm]
sel. 0.8	-2.438 ± 0.005	-2.438 ± 0.005	-2.438 ± 0.005	-2.439 ± 0.005	-2.440 ± 0.005
sel. 0.9	-2.390 ± 0.005	-2.392 ± 0.005	-2.390 ± 0.005	-2.390 ± 0.005	-2.390 ± 0.005
sel. 1.0	-2.349 ± 0.005	-2.350 ± 0.005	-2.349 ± 0.005	-2.348 ± 0.005	-2.349 ± 0.005
sel. 1.1	-2.326 ± 0.005	-2.325 ± 0.005	-2.324 ± 0.005	-2.326 ± 0.005	-2.327 ± 0.005
sel. 1.2	-2.316 ± 0.005	-2.314 ± 0.005	-2.313 ± 0.005	-2.315 ± 0.005	-2.316 ± 0.005
sel. 1.3	-2.311 ± 0.005	-2.310 ± 0.005	-2.311 ± 0.005	-2.312 ± 0.005	-2.312 ± 0.005
sel. 2.5	-2.311 ± 0.005	-2.310 ± 0.005	-2.311 ± 0.005	-2.311 ± 0.005	-2.312 ± 0.005

Table D.1: The result of TProfile method on MC from station 3.

sel. 0.8	-2.439 ± 0.005
sel. 0.9	-2.390 ± 0.005
sel. 1.0	-2.349 ± 0.005
sel. 1.1	-2.326 ± 0.005
sel. 1.2	-2.315 ± 0.005
sel. 1.3	-2.311 ± 0.005
sel. 2.5	-2.311 ± 0.005

Table D.2: Weighted average over bin sizes for TProfile method on MC for station 3.

bin width	0.010 [mm]	0.015 [mm]	0.020 [mm]	0.025 [mm]	0.050 [mm]
sel. 1.20	-2.375 ± 0.002	-2.377 ± 0.002	-2.376 ± 0.002	-2.378 ± 0.002	-2.381 ± 0.002
sel. 1.40	-2.256 ± 0.001	-2.259 ± 0.001	-2.258 ± 0.001	-2.258 ± 0.001	-2.259 ± 0.001
sel. 1.60	-2.228 ± 0.001	-2.230 ± 0.001	-2.230 ± 0.001	-2.229 ± 0.001	-2.230 ± 0.001
sel. 1.80	-2.234 ± 0.001	-2.236 ± 0.001	-2.235 ± 0.001	-2.236 ± 0.001	-2.234 ± 0.001
sel. 2.00	-2.248 ± 0.001	-2.250 ± 0.001	-2.249 ± 0.001	-2.250 ± 0.001	-2.249 ± 0.001
sel. 2.25	-2.269 ± 0.001	-2.270 ± 0.001	-2.270 ± 0.001	-2.271 ± 0.001	-2.270 ± 0.001
sel. 2.50	-2.292 ± 0.001	-2.293 ± 0.001	-2.293 ± 0.001	-2.292 ± 0.001	-2.292 ± 0.001

Table D.3: The result of TProfile method on data from station 3.

sel. 1.20	-2.377 ± 0.002
sel. 1.40	-2.258 ± 0.001
sel. 1.60	-2.229 ± 0.001
sel. 1.80	-2.235 ± 0.001
sel. 2.00	-2.249 ± 0.001
sel. 2.25	-2.270 ± 0.001
sel. 2.50	-2.292 ± 0.001

Table D.4: Average over bin sizes for TProfile method on data for station 3.

bin width	0.010 [mm]	0.015 [mm]	0.020 [mm]	0.025 [mm]	0.050 [mm]
sel. 0.8	-2.479 ± 0.005	-2.475 ± 0.005	-2.477 ± 0.005	-2.476 ± 0.005	-2.474 ± 0.006
sel. 0.9	-2.467 ± 0.006	-2.465 ± 0.006	-2.467 ± 0.006	-2.469 ± 0.006	-2.466 ± 0.006
sel. 1.0	-2.460 ± 0.007	-2.458 ± 0.007	-2.459 ± 0.007	-2.459 ± 0.007	-2.459 ± 0.007
sel. 1.1	-2.455 ± 0.007	-2.454 ± 0.007	-2.455 ± 0.007	-2.455 ± 0.007	-2.454 ± 0.007
sel. 1.2	-2.454 ± 0.007	-2.453 ± 0.007	-2.454 ± 0.007	-2.454 ± 0.007	-2.453 ± 0.007
sel. 1.3	-2.454 ± 0.007	-2.453 ± 0.007	-2.454 ± 0.007	-2.453 ± 0.007	-2.453 ± 0.007
sel. 2.5	-2.454 ± 0.007	-2.453 ± 0.007	-2.454 ± 0.007	-2.453 ± 0.007	-2.453 ± 0.007

Table D.5: The result of FitSlices method on MC from station 3.

sel. 0.8	-2.476 ± 0.006
sel. 0.9	-2.469 ± 0.006
sel. 1.0	-2.359 ± 0.007
sel. 1.1	-2.355 ± 0.007
sel. 1.2	-2.354 ± 0.007
sel. 1.3	-2.453 ± 0.007
sel. 2.5	-2.353 ± 0.007

Table D.6: Weighted average over bin sizes for FitSlices method on MC for station 3.

bin width	0.010 [mm]	0.015 [mm]	0.020 [mm]	0.025 [mm]	0.050 [mm]
sel. 1.20	-2.325 ± 0.002	-2.325 ± 0.002	-2.325 ± 0.002	-2.326 ± 0.002	-2.326 ± 0.002
sel. 1.40	-2.153 ± 0.004	-2.155 ± 0.004	-2.153 ± 0.004	-2.153 ± 0.004	-2.158 ± 0.003
sel. 1.60	-2.172 ± 0.003	-2.171 ± 0.003	-2.171 ± 0.003	-2.168 ± 0.003	-2.173 ± 0.003
sel. 1.80	-2.204 ± 0.002	-2.204 ± 0.002	-2.204 ± 0.002	-2.201 ± 0.002	-2.207 ± 0.002
sel. 2.00	-2.210 ± 0.002	-2.211 ± 0.002	-2.210 ± 0.002	-2.210 ± 0.002	-2.207 ± 0.002
sel. 2.25	-2.212 ± 0.002	-2.214 ± 0.002	-2.212 ± 0.002	-2.213 ± 0.002	-2.210 ± 0.002
sel. 2.50	-2.214 ± 0.002	-2.213 ± 0.002	-2.213 ± 0.002	-2.215 ± 0.002	-2.211 ± 0.002

Table D.7: The result of FitSlices method on data from station 3.

sel. 1.20	-2.325 $\pm$ 0.002
sel. 1.40	-2.154 $\pm$ 0.004
sel. 1.60	-2.171 $\pm$ 0.003
sel. 1.80	-2.204 $\pm$ 0.002
sel. 2.00	-2.210 $\pm$ 0.002
sel. 2.25	-2.212 $\pm$ 0.002
sel. 2.50	-2.213 $\pm$ 0.002

Table D.8: Average over bin sizes for FitSlices method on data for station 3.

selection		1.20	1.40	1.60	1.80	2.00	2.25	2.50	1.20	1.40	1.60	1.80	2.00	2.25	2.50
	results	-2.377	-2.377	-2.229	-2.235	-2.249	-2.270	-2.292	-2.325	-2.154	-2.171	-2.204	-2.210	-2.212	-2.213
0.8	-2.439	0.620	0.620	0.210	0.204	0.190	0.169	0.147	0.114	0.285	0.268	0.235	0.229	0.227	0.226
0.9	-2.390	0.013	0.013	0.161	0.155	0.141	0.120	0.098	0.065	0.236	0.219	0.186	0.180	0.178	0.177
1.0	-2.349	0.028	0.028	0.120	0.114	0.100	0.079	0.057	0.024	0.195	0.178	0.145	0.139	0.137	0.136
1.1	-2.326	0.051	0.051	0.097	0.091	0.077	0.056	0.034	0.001	0.172	0.155	0.122	0.116	0.114	0.113
1.2	-2.315	0.062	0.062	0.086	0.080	0.066	0.045	0.023	0.010	0.161	0.144	0.111	0.105	0.103	0.102
1.3	-2.311	0.066	0.066	0.082	0.076	0.062	0.041	0.019	0.014	0.157	0.140	0.107	0.101	0.099	0.098
2.5	-2.311	0.066	0.066	0.082	0.076	0.062	0.041	0.019	0.014	0.157	0.140	0.107	0.101	0.099	0.098
0.8	-2.476	0.099	0.099	0.247	0.241	0.227	0.206	0.184	0.151	0.322	0.305	0.272	0.266	0.264	0.263
0.9	-2.469	0.092	0.092	0.240	0.234	0.220	0.199	0.177	0.144	0.315	0.298	0.265	0.259	0.257	0.256
1.0	-2.359	0.018	0.018	0.130	0.124	0.110	0.089	0.067	0.034	0.205	0.188	0.155	0.149	0.147	0.146
1.1	-2.355	0.022	0.022	0.126	0.120	0.106	0.085	0.063	0.030	0.201	0.184	0.151	0.145	0.143	0.142
1.2	-2.354	0.023	0.023	0.125	0.119	0.105	0.084	0.062	0.029	0.200	0.183	0.150	0.144	0.142	0.141
1.3	-2.353	0.024	0.024	0.124	0.118	0.104	0.083	0.061	0.028	0.199	0.182	0.149	0.143	0.141	0.140
2.5	-2.353	0.024	0.240	0.124	0.118	0.104	0.830	0.610	0.280	0.199	0.182	0.149	0.143	0.141	0.140

Table D.9: Diffrences between data and MC for station 3.

Bibliography

[1] S. Benedetti et al. “The 2017 Xe run at CERN Linac3: Measurements and beam dynamics simulations”. In: *Review of Scientific Instruments* 89.12 (2018), p. 123301. DOI: 10.1063/1.5066086. eprint: https://doi.org/10.1063/1.5066086. URL: https://doi.org/10.1063/1.5066086.

[2] C Hill et al. “Performance of the CERN Linac 2 with a high intensity proton RFQ”. In: (Oct. 1994).

[3] L. Arnaudon et al. “Linac4 technical design report”. In: (Dec. 2006).

[4] CERN Collaboration. *CLEAR*. URL: https://clear.cern/content/welcome-clear.

[5] Günther Plass. *Design study of a facility for experiments with low energy antiprotons (LEAR)*. Geneva: CERN, 1980. URL: https://cds.cern.ch/record/124681.

[6] Edouard Regenstreif. *The CERN Proton Synchrotron*. CERN Yellow Reports: Monographs. French version published as CERN 61-09. Geneva: CERN, 1962. DOI: 10.5170/CERN-1962-003. URL: https://cds.cern.ch/record/278715.

[7] I. Ambats et al. “The MINOS Detectors Technical Design Report”. In: (Oct. 1998).

[8] S A Baird et al. *Design study of the antiproton decelerator: AD*. Tech. rep. CERN-PS-96-043-AR. Nov. 1996. URL: https://cds.cern.ch/record/317704.

[9] A Caldwell et al. *AWAKE Design Report: A Proton-Driven Plasma Wakefield Acceleration Experiment at CERN*. Tech. rep. CERN-SPSC-2013-013. SPSC-TDR-003. Apr. 2013. URL: https://cds.cern.ch/record/1537318.

[10] Andrew J et al. *The Large Hadron Collider*. DOI: 10.1142/q0040. URL: https://www.worldscientific.com/doi/abs/10.1142/q0040.

[11] Michael Benedikt et al. *LHC Design Report*. CERN Yellow Reports: Monographs. Geneva: CERN, 2004. DOI: 10.5170/CERN-2004-003-V-3. URL: https://cds.cern.ch/record/823808.

[12] CERN Collaboration. *The CERN accelerator complex*. URL: https://cds.cern.ch/record/2684277/files/.

[13] B. Auchmann et al. *Testing Beam-Induced Quench Levels of LHC Superconducting Magnets*. DOI: 10.1103/PhysRevSTAB.18.061002.

[14] L. Rossi and E. Todesco. *Conceptual design of 20 T dipoles for high-energy LHC*. DOI: 10.5170/CERN-2011-003.13.

[15] F. Bonaudi. *Magnets in particle physics*. URL: https://cds.cern.ch/record/245397/files/p1.pdf.

[16] Wikipedia. *An lhc dipole magnet in Belgrade*. URL: https://upload.wikimedia.org/wikipedia/commons/6/62/Closer_look_at_an_lhc_dipole_magnet_in_belgrade.jpg.

[17] CERN collaboration. *Magnetic multipoles*. URL: https://www.lhc-closer.es/taking_a_closer_look_at_lhc/0.magnetic_multipoles.

[18] *Observation of a new particle in the search for the Standard Model Higgs boson with the ATLAS detector at the LHC*. DOI: j.physletb.2012.08.020.

[19] Alexander V. Zlobin. *Superconducting Magnets - Principles, Operation, and Applications*. ISBN: 9780471346081. DOI: 10.1002/047134608X.W4520.

[20] *Technical Design Report for the ATLAS Inner Tracker Pixel Detector*. Tech. rep. CERN-LHCC-2017-021. ATLAS-TDR-030. Geneva: CERN, Sept. 2017. URL: https://cds.cern.ch/record/2285585.

[21] The ATLAS collaboration. *A study of the material in the ATLAS inner detector using secondary hadronic interactions*. DOI: 10.1088/1748-0221.

[22] The ATLAS collaboration. *Study of the material of the ATLAS inner detector for Run 2 of the LHC*. DOI: 10.1088/1748-0221/12/12/p12009. URL: https://doi.org/10.1088%2F1748-0221%2F12%2F12%2Fp12009.

[23] The ATLAS collaboration. *Performance of the electronic readout of the ATLAS liquid argon calorimeters*. DOI: 10.1088/1748-0221/5/09/p09003.

[24] *Technical Design Report for the Phase-II Upgrade of the ATLAS Tile Calorimeter*. Tech. rep. CERN-LHCC-2017-019. ATLAS-TDR-028. Geneva: CERN, Sept. 2017. URL: https://cds.cern.ch/record/2285583.

[25] *Technical Design Report for the Phase-II Upgrade of the ATLAS Muon Spectrometer*. Tech. rep. CERN-LHCC-2017-017. ATLAS-TDR-026. Geneva: CERN, Sept. 2017. URL: https://cds.cern.ch/record/2285580.

[26] E. Diehl. *Calibration and Performance of the ATLAS Muon Spectrometer*. eprint: 1109.6933.

[27] Joao Pequenao. *Computer generated image of the whole ATLAS detector*. URL: https://cds.cern.ch/record/1095924.

[28] G. Avoni, M. Bruschi, and G. Cabras. *The new LUCID-2 detector for luminosity measurement and monitoring in ATLAS*. DOI: 10.1088/1748-0221/13/07/p07017.

[29] Christophe Royon. *The ATLAS Forward Physics Program*. DOI: 10.22323/1.106.0088.

[30] Rhys Edward Owen. *The ATLAS Trigger System*. URL: https://cds.cern.ch/record/2302730.

[31] G. Antchev. *Diffraction at TOTEM*. DOI: 10.3204/DESY-PROC-2009-02/20.

[32] M.B. Gay Ducati and Goncalves. *The Hard and soft contributions on diffraction: A Closer look*. DOI: 10.1016/S0370-2693(01)00406-3.

[33] Maciej Trzebinski. *Prospects for Proton-Proton Measurements with Tagged Protons in ATLAS*. eprint: 1909.10827.

[34] AFP colaboration. *General scheme of AFP detectors*. URL: https://twiki.cern.ch/twiki/bin/view/Atlas/AFP_Figures.

[35] Nitesh Soni. *ATLAS Forward Detectors and Physics*. eprint: 1006.5426.

[36] L Adamczyk et al. *Technical Design Report for the ATLAS Forward Proton Detector*. Tech. rep. CERN-LHCC-2015-009. ATLAS-TDR-024. May 2015. URL: https://cds.cern.ch/record/2017378.

[37] S. Grinstein. *The ATLAS Forward Proton Detector (AFP)*. DOI: j.nuclphysbps.2015.09.185.

[38] S. Abdel Khalek et al. *The ALFA Roman Pot Detectors of ATLAS*. DOI: 10.1088/1748-0221/11/11/P11013.

[39] Pawel Buglewicz. *Hot-spot Method for Alignment of Forward Proton Detectors at the LHC*. DOI: 10.5506/APhysPolB.47.1619.